Article

Specific expansion of motor cortical projections in a singing mouse

https://doi.org/10.1038/s41586-026-10458-y

Received: 27 November 2024

Accepted: 26 March 2026

Published online: 06 May 2026

Open access

Check for updates

Emily C. Isko[1,2], Clifford E. Harpole[1], Xiaoyue Mike Zheng[1,2], Huiqing Zhan[1], Martin B. Davis[1], Anthony M. Zador[1,2]✉ & Arkarup Banerjee[1,2]✉

Elucidating how modifications in neural circuit architecture drive behavioural innovation remains a key challenge in neuroscience and evolutionary biology. In mammals, the neocortex is posited to play a crucial part in facilitating rapid behavioural innovations[1–3]. Although changes in long-range connectivity have been proposed to underlie such innovations[4,5], these hypotheses remain largely untested quantitatively, which is partly due to the lack of high-throughput neuronal projection data at single-neuron resolution across species. Here we studied the Alston's singing mouse (*Scotinomys teguina*), which exhibits a striking vocal behaviour absent in the laboratory mouse (*Mus musculus*), to quantitatively determine species-specific changes in motor cortical projections throughout the brain. We used bulk tracing, serial two-photon tomography and high-throughput DNA sequencing of more than 76,000 barcoded neurons to discover a specific and substantial expansion of orofacial motor cortical projections to an auditory cortical region and the midbrain periaqueductal grey, regions that are implicated in vocal behaviours[6–9]. Moreover, analyses of projection motifs of individual orofacial motor cortical neurons revealed preferential expansion of exclusive projections to the auditory cortical region in the singing mouse. Our results suggest that selective expansion of ancestral motor cortical projections may lead to behavioural divergence over short timescales. Furthermore, the results facilitate mechanistic investigations of enhanced cortical control over vocalizations—a crucial preadaptation for human language[10,11]. This approach of comparing recently diverged species with substantial behavioural divergences can be readily generalized across other model clades to discover quantitative rules of neural circuit evolution.

The origins of diverse behavioural traits have fascinated biologists for centuries. Such behavioural diversity prompts an essential question in neuroscience: how neural circuits are modified to generate novel behaviours. The role of the neocortex, which is a defining feature of mammalian brain evolution, is particularly relevant for behavioural innovations[1,2]. The overall organizational plan of the cortex is markedly conserved; however, this gross similarity belies the species-specific cellular and circuit modifications that underlie the enormous diversity of behaviours among mammals[3]. Deciphering the rules by which cortical architecture evolves is key to understanding how it drives behavioural innovations.

Multiple models of how brains change through time at different spatiotemporal scales have been proposed[5,12–17]. Over long timescales, cortical evolution is probably fuelled by changes in the absolute or relative sizes of the cortical fields[3] and in the changes in numbers, composition and spatial distribution of cell types[18]. Substantial evidence exists for each of these models. For example, the primate cortex compared to that of a rodent shows a massive expansion in cortical field sizes[19], increased dendritic arborization[20] and even an interneuron cell type not found in mice and ferrets[21]. Beyond such changes in brain architecture, other influential models predict that modified long-range connectivity among existing brain regions can lead to functional divergences[4,5,22,23]. These processes can lead to species-specific connections not seen in the ancestral circuit or quantitative changes in preexisting projections. However, these models of inter-areal cortical connectivity have not been tested quantitatively and, in general, mechanisms concerning rapid behavioural divergence remain poorly understood.

The paucity of empirical data to test these models is partially due to technical challenges. Current neuroanatomical methods involve trade-offs between resolution and scalability. Bulk viral tracing of projection patterns can detect previously unknown projections[4,23,24] but does not provide quantitative analyses of projection collaterals. At the other extreme, electron-microscopy-based connectomes[25–27] provide subcellular resolution but remain difficult to scale up for cross-species comparisons in vertebrate brains. Testing models of cortical circuit divergence would require a quantifiable behavioural difference between closely related species, an a priori knowledge of a behaviourally relevant cortical region and a technique for high-throughput

[1]Cold Spring Harbor Laboratory, Cold Spring Harbor, NY, USA. [2]School of Biological Sciences, Cold Spring Harbor Laboratory, Cold Spring Harbor, NY, USA. ✉e-mail: tzcshl@gmail.com; abanerjee@cshl.edu

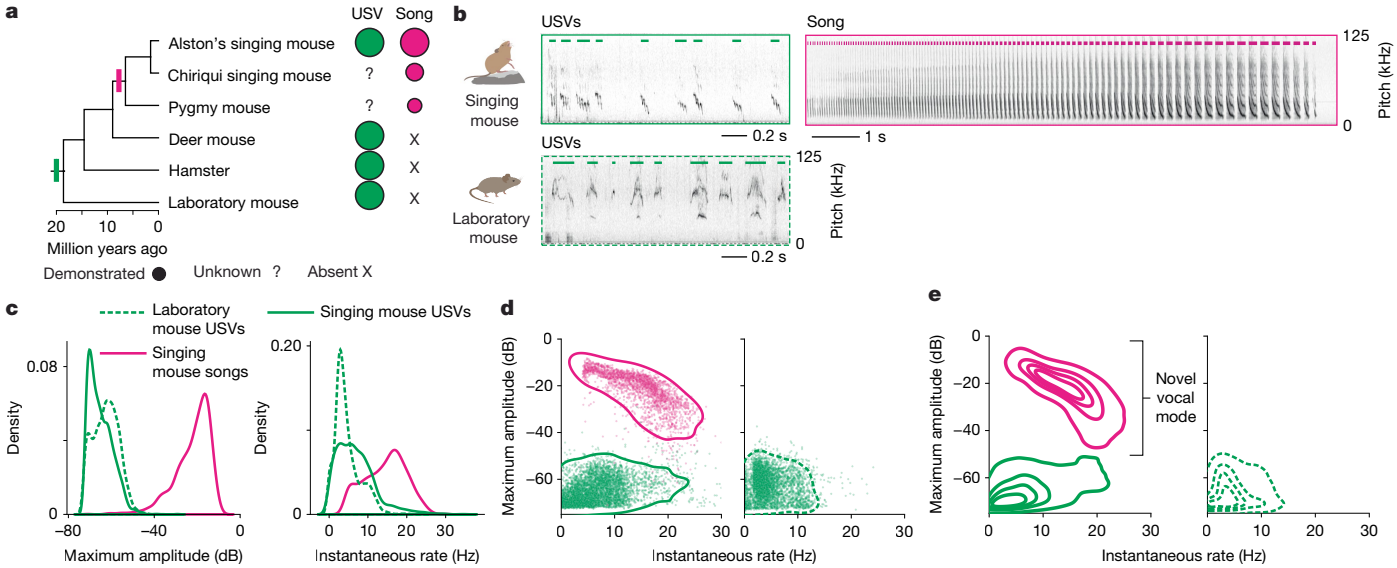

Fig. 1 | Behavioural novelty in singing mice. a, Phylogenetic relationships of select rodent species labelled by whether there is documented evidence for adult USVs and/or songs. The area of song circles indicate the mean number of notes per song (magenta circles). **b**, Example spectrograms of vocalizations from singing mice (top, solid lines) and laboratory mice (bottom, dashed line) during social interactions between male and muted female animals. Horizontal coloured bars in the spectrograms mark the duration of each vocalization. **c**, Histograms of maximum amplitude (left) and instantaneous note rate (right) of individual notes from a single pair of laboratory mice and singing mice. Notes were assigned a vocalization category based on amplitude and bout length (colour key applies to **d** and **e**). **d**, Summary of vocalizations from the same animal pair as in **c**. Each dot is a vocalization and lines represent equidensity contours. $n = 6{,}971$ notes for the singing mouse, $n = 3{,}970$ notes for the laboratory mouse. **e**, Summary of notes from five singing mice (left) and five laboratory mice (right). Contours represent the note density at five equally spaced intervals (colour key is as **c**). Singing mice display two vocalization types (left): USVs (instantaneous note rate, 0.8–16.3 Hz; normalized amplitude, −71.8 to −55.6 dB; $n = 28{,}150$ notes) and songs (instantaneous note rate, 7.0–21.5 Hz; normalized amplitude, −38.3 to −12.8 dB; $n = 9{,}934$). By contrast, laboratory mice only display a single vocalization type (right): USVs (instantaneous note rate, 0.2–11.0 Hz; normalized amplitude: −72.3 to −55.4 dB; $n = 8{,}946$). Ranges represent 5th to 95th percentile values.

mapping at single-cell resolution in many individuals. In this study, we leverage a behavioural novelty in the Alston's singing mouse (*S. teguina*) to quantitatively measure and compare brain-wide motor cortical projections using high-throughput barcoded projection mapping of thousands of neurons across multiple animals.

The Alston's singing mouse is a neotropical cricetid rodent that has emerged as a mammalian model system for studying neural mechanisms of vocal communication[28]. Singing mice produce long, stereotyped, human-audible songs[29–32] that are used for antiphonal (call-and-response) interactions that exhibit some parallels with human conversational turn-taking[33]. Based on several complementary lines of evidence, we have demonstrated that this vocal turn-taking behaviour depends on the orofacial motor cortex (OMC), an anterolateral hotspot of the motor cortex[32,34]. First, electrical stimulation of the OMC disrupted or paused ongoing singing. Second, silencing OMC activity using a $GABA_A$ agonist (muscimol) significantly decreased turn-taking. Third, mild focal cooling of the OMC increased song duration. Finally, we showed that temporal scaling of OMC neural dynamics, acting through downstream motor production circuits, can control song duration. Maps of the OMC, generated using intracortical microstimulation, spatially overlap in laboratory mice (*M. musculus*)[35,36] and singing mice[32]. Laboratory mice, which separated from singing mice around 18 million years ago[37] (Fig. 1a), produce ultrasonic vocalizations (USVs) and differ from singing mice in that they do not seem to display turn-taking[33].

Here we first show that the singing mouse has evolved a novel vocal mode (songs) while retaining USVs ancestral to rodents. We then quantitatively test models of motor cortical divergence between the two species. Using bulk tracing, serial two-photon tomography (STPT) and high-throughput DNA sequencing of thousands of barcoded neurons, we demonstrate that there is selective expansion of OMC projections in the singing mouse to two specific downstream targets: an auditory region (AudR) and the midbrain periaqueductal grey (PAG). Our results suggest that large behavioural divergences over short timescales may not require drastic modifications in brain architecture but may instead proceed by modifying statistics of long-range projection patterns.

Behavioural novelty in the singing mouse

We began by quantifying the phenotypic (behavioural) divergence between the two rodent species in identical contexts. We paired males ($n = 5$ singing mice, $n = 5$ laboratory mice) with conspecific, muted females and allowed them to interact freely in a behavioural chamber for 1 h while continuously recording their vocalizations. This paradigm elicited robust vocalizations in both species (38,084 vocalizations for singing mice and 8,946 vocalizations for laboratory mice), which enabled precise assignment and quantitative assessment of their acoustic features. Consistent with previous reports, male laboratory mice produced USVs in this affiliative behavioural context (Fig. 1b–d and Supplementary Video 1).

By contrast, vocalizations by singing mice showed two distinct clusters (Fig. 1b–d and Supplementary Video 2). One cluster consisted of loud, stereotyped song notes, whereas the other cluster corresponded to quieter, more variable vocalizations. This quieter cluster overlapped with the corresponding USV cluster from the laboratory mice (Fig. 1c,d). Given that there are multiple reports of adult USVs in a variety of rodent species, such as hamsters (*Mesocricetus auratus*)[38] and deer mice (*Peromyscus californicus* and *Peromyscus boylii*)[39], we infer that these USVs can be considered an ancestral trait (Fig. 1a). The second cluster of louder notes in the singing mice followed a stereotyped temporal sequence over many seconds (that is, songs; Extended Data Fig. 1). Unlike USVs, songs were approximately 40 dB louder (Fig. 1 and Extended Data Fig. 1) and are used for long-distance turn-taking[32,40], which substantially expands the vocal reach of this species to tens of metres. Singing seems to be exclusive to the Baiomyini clade, including Chiriqui singing mice (*Scotinomys xerampelinus*)[30] and pygmy mice

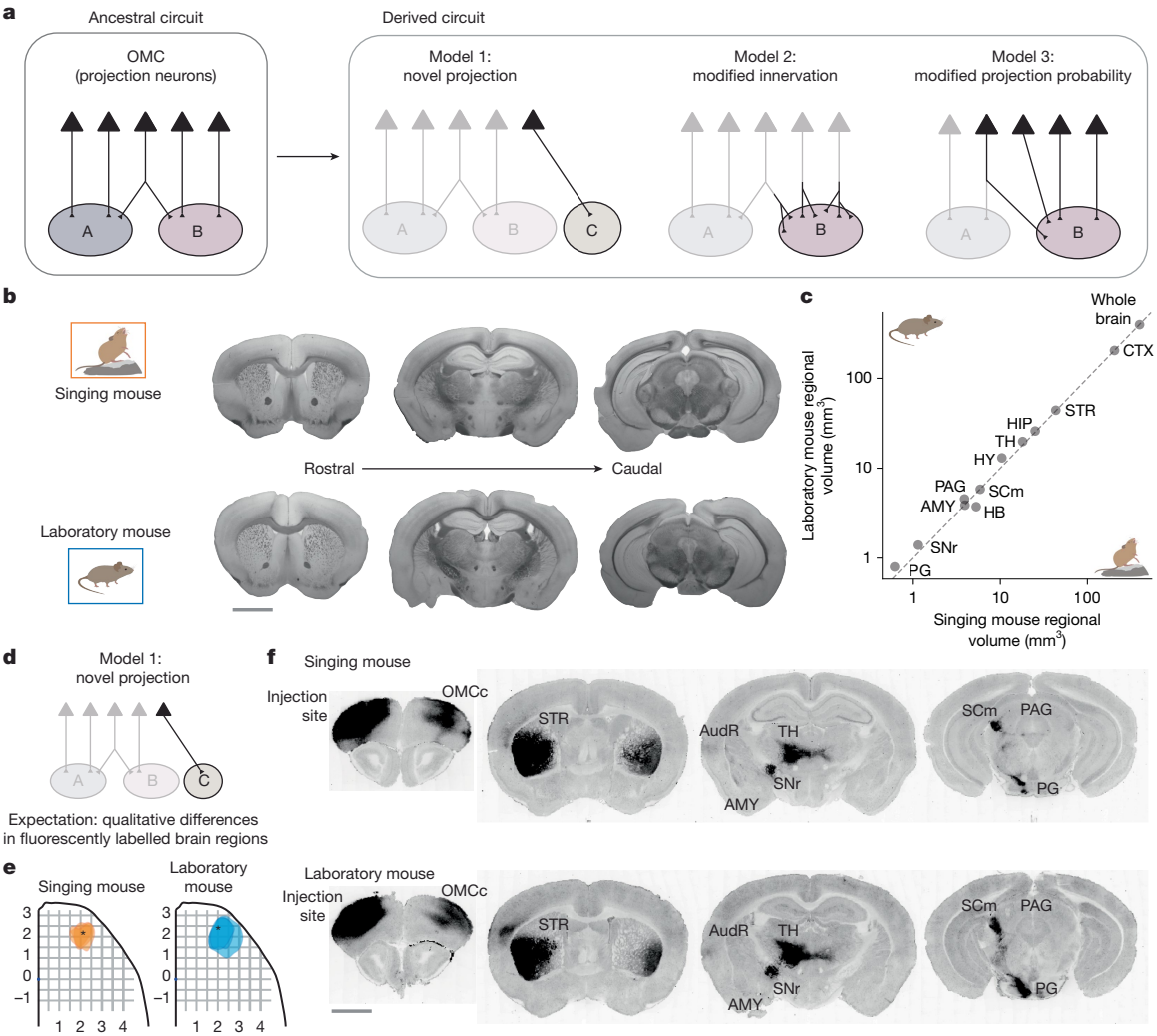

Fig. 2 | Testing models of motor cortical divergence across species. **a**, Schematic of three possible models by which OMC projections derived from an ancestral circuit can differ between the two species. **b**, Comparison of gross anatomical structures of matched coronal sections from both species imaged using bright-field microscopy. **c**, Comparisons of volumes of selected brain regions in laboratory mice and singing mice. **d**, Schematic of testing model 1: identification of novel OMC projection targets by viral tracing of axonal projections. **e**, Targeting of the homologous OMC regions in both species based on previous studies and overlay of OMC viral spread in singing mice (left, $n = 3$) and laboratory mice (right, $n = 3$). Asterisks mark the centre of the injection sites (laboratory mice[35,36]; singing mice[32]). **f**, Comparison of brain-wide fluorescence distributions of OMC axonal projections across matched coronal sections from both species. For the full dataset of three laboratory and three singing mice, see Extended Data Figs. 2 and 3. Scale bars, 2 mm (**b**,**f**). AMY, amygdala; CTX, cortex; HB, hindbrain; HIP, hippocampus; HY, hypothalamus; PG, pontine grey; SCm, superior colliculus motor; TH, thalamus.

(*Baiomys taylori*)[30]. In this lineage, Alston's singing mice produce the most elaborate version of this novel trait: the loudest and longest songs with the fastest note rates[30].

Taken together, we posit that USV is the ancestral phenotype and that songs are a novel phenotype in the Baiomyini clade. Furthermore, laboratory mice and Alston's singing mice are good representative species to further explore evolving circuits that underlie this behavioural innovation.

Testing models of brain-wide cortical projections

Building on previous functional results[32,34], we wondered whether species-typical differences in vocal behaviours between laboratory mice and singing mice arise from differential projection patterns of OMC neurons. Although not an exhaustive list, we tested three possible models for wiring changes that would result in differential neural circuit function. First, OMC neurons in singing mice project to target regions not seen in laboratory mice (model 1; Fig. 2a, second from left). Alternatively, OMC neurons project to the same brain regions in both species but differ in the amount of axonal material per neuron in target regions, referred to as innervation strength (model 2; Fig. 2a, second from right). Finally, neurons project to the same brain regions in both species but differ in the probability that a neuron projects to the target brain region (model 3; Fig. 2a, right).

To test the hypothesis that novel projections exist from the OMC in either species, we first measured bulk axonal projection patterns. We injected AAV2.9-CaMKII-tdTomato into the OMC of laboratory and singing mice ($n = 3$ for each species) and used STPT to obtain an unbiased map of OMC projections throughout the entire brain. Laboratory and singing mouse brains looked nearly identical in gross morphology, as illustrated by three representative coronal sections (Fig. 2b and Supplementary Videos 3 and 4). We did not find significant differences in the overall volume or allometric scaling of the OMC or other brain regions among the two species (Fig. 2c). Relying on this gross morphological similarity, we aligned all brains to a reference singing mouse brain and compared fluorescence distributions (Fig. 2d–f, Methods and Extended Data Figs. 2 and 3). OMC neurons from both species targeted the same downstream regions (Fig. 2f and Supplementary Videos 3 and 4) and

matched previously reported motor cortical connectivity in the laboratory mouse[41,42]. Thus, we conclude that overall brain architecture and projection patterns of OMC neurons are qualitatively similar between the two species.

In the absence of novel projections, we next wondered whether anatomical differences between the species exist at the single-cell level. Although bulk axonal tracing experiments can map brain-wide projection patterns, this technique cannot resolve quantitative differences in single-neuron projections patterns. Therefore, we used multiplexed analysis of projections by sequencing (MAPseq) to map the projection targets of thousands of motor cortical neurons simultaneously at single-cell resolution[43]. MAPseq experiments involve uniquely tagging thousands of neurons with distinct RNA barcodes through injection of a diverse library of barcoded Sindbis virus. The barcodes are expressed and then actively transported into the axonal processes of each labelled neuron. Target regions identified in bulk tracing (Fig. 2f and Methods) are then dissected (Supplementary Figs. 1 and 2), and barcodes are extracted and analysed by high-throughput barcode sequencing (Fig. 3a).

In classical neuronal viral tracing, a fluorescent protein (for example, GFP) is expressed and its fluorescence can be used to track the volumes of neuronal axons. MAPseq takes a similar approach, except that instead of filling the neuron with a fluorescent protein, the neuron is filled with a unique RNA barcode. The abundance of each barcode sequence (that is, expression level) in each area serves as a measure of the extent of axonal processes of a given cell in a specific target region. MAPseq has been repeatedly validated in multiple studies using multiple methodologies[41,43,44] (Methods) but has not been used to test models of species-specific changes in neural circuitry. The high-throughput and single-cell resolution capacity of MAPseq make it ideally suited to analyse quantitative differences in brain-wide projection patterns across species.

Using MAPseq, we were able to recover thousands of single-neuron projection patterns in singing and laboratory mice (Fig. 3b, $n = 5{,}114$ neurons from 7 singing mice; $n = 71{,}704$ neurons from 5 laboratory mice). The expression level of barcodes in infected neurons was similar between species, which indicated comparable sensitivity, although the number of recovered unique barcodes per animal differed. In detail, there were 0.04 ± 0.02 (mean ± s.e.m.) normalized expression of barcodes for laboratory mice compared with 0.13 ± 0.04 for singing mice, and 14,000 ± 2,500 unique barcodes per animal for laboratory mice and 700 ± 100 for singing mice (Methods and Extended Data Fig. 4). Analyses of MAPseq projection patterns confirmed previous reports[41] of three major excitatory cortical neurons: intratelencephalic (IT) neurons, which project within the cortex and to the striatum (STR); corticothalamic (CT) neurons, which project from the cortex to the thalamus; and pyramidal tract (PT) neurons, which project from the cortex to the midbrain and hindbrain (Fig. 3b).

In the absence of qualitative differences, we tested the hypothesis that OMC neurons project to the same brain regions in both species but differ in the strength of innervation in the target regions. To determine this possibility, we compared normalized barcode expression per neuron (Methods) across areas and between species (Fig. 3c–e). The barcode expression per neuron is proportional to the total axonal volume in the target region, much like a fluorescent protein (for example, GFP) used in conventional anatomical tracing experiments[44]. We did not find any target brain region with significant differences in the median barcode expression per neuron (Fig. 3e). Therefore, we conclude that there are no significant differences in the strength of innervation of OMC neurons to downstream target regions between the two species.

Finally, we tested the hypothesis that the species difference lies in the probability (*Prob*) of OMC neurons projecting to downstream target brain regions. We calculated the proportion of OMC neurons that project to specific target regions in IT and PT neurons separately (Fig. 3f–h). Consistent with previous reports[41], IT neurons from the OMC projected heavily to the STR ($Prob_{STR} = 0.91 \pm 0.02$) and the contralateral OMC (OMCc) ($Prob_{OMCc} = 0.78 \pm 0.04$), whereas PT neurons exhibited strong projections to many regions, including the pontine grey ($Prob_{PG} = 0.66 \pm 0.03$), the substantia nigra (SNr) ($Prob_{SNr} = 0.50 \pm 0.10$) and many other subcortical brain regions. For most brain regions (9 out of 11, 82%), we did not observe differences in the projection probability of IT or PT neurons between the two species. The observed differences were in one IT target (the AudR, including the primary and secondary auditory cortex) and one PT target (the PAG). The projection probability of OMC IT neurons to the AudR was significantly higher (2.8-fold) in singing mice than in laboratory mice (0.05 ± 0.05 for laboratory mice compared with 0.14 ± 0.06 for singing mice, $P = 0.03$ Mann–Whitney *U*-test). Similarly, 40% of all OMC PT neurons in singing mice projected to the PAG compared with only 12% in laboratory mice. This result represented a significant (3.3-fold) increase in projection probability (0.12 ± 0.14 in laboratory mice compared with 0.40 ± 0.12 in the singing mice, $P = 0.03$ Mann–Whitney *U*-test; Fig. 3h).

We next wondered whether this expanded projection is sexually dimorphic. Both male and female singing mice produced songs with overlapping distributions of loudness and note rate (Extended Data Fig. 5a,b). Furthermore, both male and female singing mice have been shown to take turns with conspecifics[45]. Moreover, the quantitative difference in song durations can be accounted for by circulating androgen levels[46]. Therefore, we did not anticipate major anatomical differences in OMC projections between male and female singing mice. Consistent with this, we found that OMC projections in both male and female singing mice were increased compared with both male and female laboratory mice (Extended Data Fig. 5c).

We subsequently validated our MAPseq results with further analyses and experiments. First, our results did not depend on the exact choice of unique molecular identifier threshold used to binarize the MAPseq projection data (Extended Data Fig. 5d,e), nor could they be explained by infectivity differences between the two species (Extended Data Fig. 4c). Second, using the whole-brain STPT data, we quantified the volume of the axonal fluorescent signal in target regions normalized to the injection site volume in each animal. This metric is equivalent to the projection probability calculated for MAPseq. In concordance with our MAPseq data, both the AudR and PAG showed increased projections in singing mice compared with laboratory mice. Notably, neither the OMCc nor the SNr (used as negative control regions) differed significantly between the two species (Extended Data Fig. 6). Third, to ensure that the OMC projections to the AudR and PAG do not simply represent passing fibres, we confirmed the presence of synaptic boutons in these regions using a synaptophysin-mRuby viral construct (Extended Data Fig. 7). Anterograde trans-synaptic mapping also confirmed the presence of putative postsynaptic neurons (Extended Data Fig. 8). Taken together, these analyses and experiments lend further support to our MAPseq results.

In summary, we identified a significant expansion of OMC projections to an AudR and the midbrain PAG in singing mice. Notably, both the AudR and PAG have been implicated in vocal communication behaviour across a variety of mammalian species[6–9,47].

Analysis of OMC projection motifs

So far, we have shown that there is significantly higher projection probabilities of OMC neurons to the PAG and AudR in singing mice than in laboratory mice. Although this finding characterizes OMC projections at the population level, it does not describe the single-neuron projection patterns that underlie these differences (Fig. 4a). Each neuron has a characteristic projection pattern in a space defined by the number of target regions. For example, an OMC IT neuron in our dataset projecting to potentially three downstream targets can exhibit any one of seven possible motifs ($2^3 - 1 = 7$), which constitute its full projectome. The total

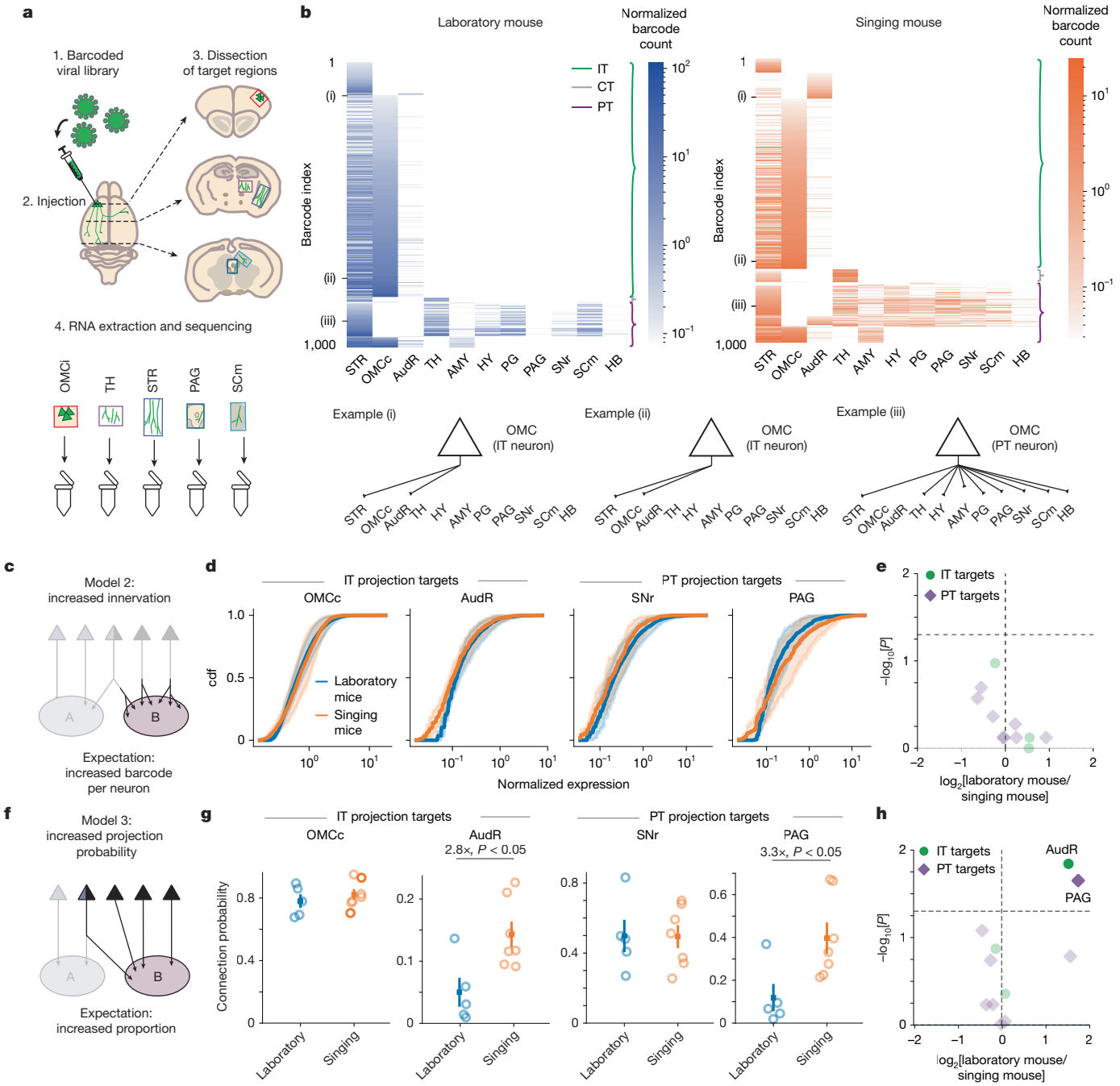

Fig. 3 | Using MAPseq to test models of projection pattern divergence between laboratory and singing mice. a, Schematic of the workflow of MAPseq (Methods). OMCi, ipsilateral OMC. **b**, Top, single-cell projection patterns of 1,000 neurons from a laboratory mouse (left) and a singing mouse (right) showing the major excitatory cell types: IT, CT and PT neurons. Bottom, single-cell projection patterns for three example ((i)–(iii)) OMC neurons. **c**, Schematic of the innervation mode (model 2). **d**, Normalized barcode expression levels per neuron for laboratory mice ($n = 5$) and singing mice ($n = 7$) for four brain regions plotted as cumulative distribution functions (cdf). Solid lines correspond to averages across individuals and shaded regions correspond to s.e.m. OMCc, laboratory = 0.50 ± 0.12, singing = 0.73 ± 0.22, $P = 0.76$. AudR, laboratory = 0.13 ± 0.02, singing = 0.11 ± 0.02, $P = 0.11$. SNr, laboratory = 0.24 ± 0.06, singing = 0.24 ± 0.07, $P = 0.76$. PAG, laboratory = 0.16 ± 0.04, singing = 0.31 ± 0.12, $P = 0.76$. Two-sided Mann–Whitney *U*-test. **e**, Volcano plot of the negative logarithm of the *P* value (two-sided Mann–Whitney *U*-test) against the fold change of normalized barcode expression between the two species for IT targets and PT targets. **f**, Schematic of projection probability (model 3). Proportions were calculated for the major cell types (for example, AudR among IT cells, PAG among PT cells). **g**, Projection probability of OMC neurons to select downstream brain regions. Each data point is an animal and colours indicate species. Solid square and vertical line denote the mean and s.e.m. respectively. OMCc, laboratory = 0.78 ± 0.04, singing = 0.82 ± 0.03, $P = 0.43$. AudR, laboratory = 0.05 ± 0.02, singing = 0.14 ± 0.02, $P = 0.03$. SNr, laboratory = 0.50 ± 0.09, singing = 0.49 ± 0.07, $P = 1.00$. PAG, laboratory = 0.12 ± 0.06, singing = 0.40 ± 0.07, $P = 0.03$. Two-sided Mann–Whitney *U*-test. **h**, Volcano plot of the negative logarithm of the *P* value (two-sided Mann–Whitney *U*-test) against the fold change of projection probabilities between the two species for IT targets and PT targets. The horizontal dashed line indicates $P = 0.05$ (two-sided Mann–Whitney *U*-test). Whole-brain illustration created by E. Thompson, adapted from SciDraw under a Creative Commons licence CC BY 4.0.

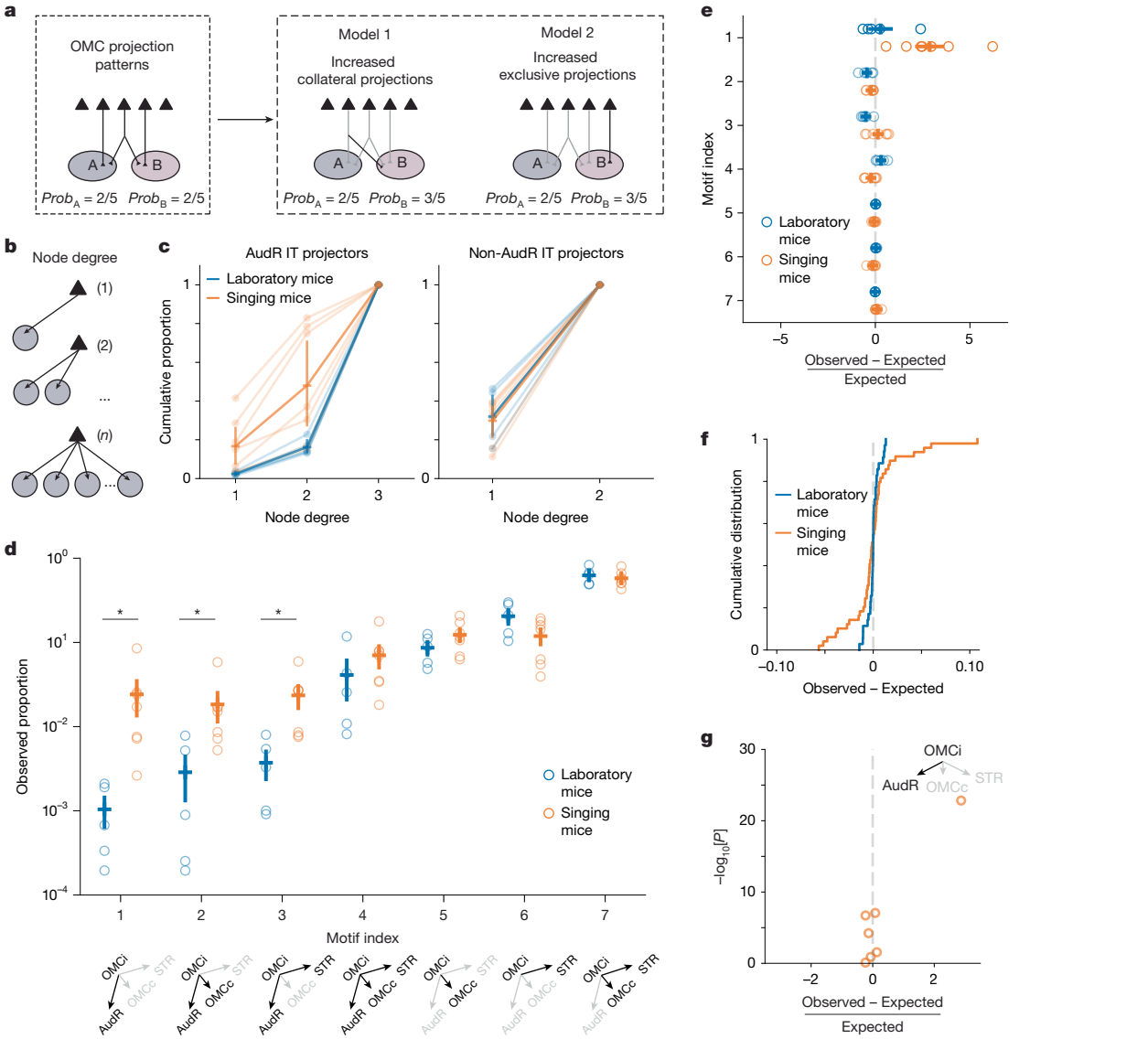

Fig. 4 | Selective expansion of long-range projection motifs in singing mice. **a**, Schematic of two models showing how increased projection probabilities could evolve from an ancestral state (left) by either increased collateral (centre) or increased exclusive (right) projections. **b**, Schematic of node degree distribution of OMC neurons. That is, the number of targets of an individual neuron. **c**, Cumulative proportion of node degrees of IT neurons that have AudR as a target (left) or do not (right). Transparent lines correspond to individual mice. Mean (opaque crosses) and s.e.m. (vertical lines) for each species. **d**, Projection probabilities for all seven OMC IT neuron motifs. Each motif is schematized below. A few select AudR-projecting motifs are expanded in the singing mice (motif 1, $P = 0.003$; motif 2, $P = 0.010$; motif 3, $P = 0.010$. Two-sided Mann–Whitney U-test). Individual mice are plotted as circles. Mean (crosses) and s.e.m. (vertical lines) values for each species are indicated. $^*P < 0.05$. **e**, Deviation of experimentally measured (observed) motif probabilities from expected values predicted under the independent binomial model (for example, $Prob_{(\text{A and B and not C})} = Prob_A \times Prob_B \times (1 - Prob_C)$) for singing mice (orange) and laboratory mice (blue). **f**, Cumulative distribution of differences between observed and expected motif probabilities across all individuals of singing mice (orange) and laboratory mice (blue). The distribution for singing mice was significantly different from that for laboratory mice ($P < 0.001$, one-sided F-test). The vertical dashed line denotes the distribution of expected motif probabilities under the binomial model. **g**, Volcano plot of observed motif probabilities for singing mice. Each data point corresponds to an individual IT neuron motif. The schematic in the inset represents the motif identity of the corresponding data point.

number of all PT motifs in our dataset is substantially larger ($2^8 - 1 = 255$), which makes it infeasible to enumerate all the individual motifs. Therefore, we restricted our subsequent analyses to the OMC IT neurons. Specifically, we aimed to identify the logic of single-neuron-level projection patterns that underlie the increased projection probability to the AudR. In one model, an increase in neural projections to a brain region could arise through increased collaterals; that is, projections to an additional target region (Fig. 4a, model 1). Alternatively, the increase could arise from neurons that project exclusively to that region (Fig. 4a, model 2). These models can be distinguished by plotting the node degree distributions, which quantifies the number of targets of each neuron. Lower node degrees indicate more exclusive projections, whereas higher node degrees indicate projections with more collaterals. In the IT population projecting to the AudR, the distribution of additional collaterals was significantly lower in singing mice than in laboratory mice (Fig. 4b,c). This result suggests that the expanded OMC projections in singing mice are preferentially mediated by axons with dedicated projections to the AudR.

To verify this possibility, we next enumerated the observed probabilities for all of the seven possible IT circuit motifs. Although we observed increased projection probabilities in singing mice for most AudR-projecting motifs, the single largest expansion was for OMC

neurons that exclusively projected to the AudR without any axon collaterals in the OMCc and STR ($P = 0.003$, Mann–Whitney U-test; Fig. 4d). Through bootstrap resampling, we again confirmed that this result cannot be explained by the mismatch in the total number of IT neurons between the two species (Extended Data Fig. 4d).

We next wondered whether the multi-areal projection statistics of OMC IT neurons can be explained using a simple binomial model. In this scenario, the probability of projecting simultaneously to multiple regions is simply given by the product of the probabilities of projecting to each region (Fig. 4e). Under this assumption of independence, the probability of single OMC neurons projecting simultaneously to two regions (AudR and OMCc) is expected to be equal to the probability of projecting to the AudR multiplied by the probability of projecting to the OMCc. For each motif in every animal, we compared the experimentally observed projection probabilities with theoretically expected projection probabilities and found overall good agreement with the binomial model predictions (Fig. 4e). Notably, deviation from the binomial model was significantly exacerbated in singing mice compared with laboratory mice ($P < 0.001$, F-test; Fig. 4f). Moreover, the greatest deviance was observed for the motif in which OMC neurons project exclusively to the AudR without collaterals to the OMCc or STR (Fig. 4e,g). We conclude that projection statistics of single OMC neurons can be explained by a simple theoretical framework, and a departure from this expectation is a sensitive measure to infer a key locus of species-specific modification. That is, exclusive OMC projections to the AudR in singing mice.

Taken together, the reduced degree distribution, the non-uniform expansion of motif probabilities and the significant deviation from the binomial expectation demonstrate that there are more OMC neurons that project exclusively or almost exclusively to the AudR in singing mice. This result suggests that simple uniform increases in neuronal projections across all motifs cannot account for the species-specific differences in single neuronal projection motifs. Rather, a selective expansion of specific long-range motor cortical projection motifs accompanies the expansion of vocal repertoire in singing mice.

Discussion

In this study, we first demonstrated that songs are a behavioural novelty in singing mice compared with laboratory mice (Fig. 1). We used this marked behavioural divergence between the two rodent species to quantitatively test models of motor cortical divergence between species (Fig. 2a). Using bulk tracing, STPT and high-throughput DNA sequencing of barcoded OMC neurons at single-cell resolution, we discovered an expansion of motor cortical output to two specific brain regions: the AudR and the midbrain PAG (Figs. 2 and 3). Using single-cell resolution analyses of thousands of cortical neurons, we further showed that this expansion is biased towards more exclusive projections to the AudR in singing mice (Fig. 4). We clearly identified a selective increase in motor cortical projections in a rodent that displays a striking vocal innovation. Such expansion of specific neuronal projections have been proposed to expand behavioural repertoire, such as increased dexterity[23,48] and courtship songs[4]. Our results suggest a possible circuit mechanism for enhanced cortical control over vocalizations.

These results highlight the utility of the singing mouse model system for testing models of neural circuit evolution. However, the general approach for testing evolutionary models as laid out here. That is, select pairs of related species with large behavioural divergence, perform functional experiments to identify brain regions causally related to the novel behaviour and subsequently investigate neural circuit differences between these species at single-cell resolution. As such, this strategy is readily applicable to other model species and clades[49].

Notably, the only two brain regions (AudR and PAG) with differential OMC innervations have been shown to be important for vocal behaviours. Note that we selected downstream OMC targets on the basis of bulk projection patterns, without any obvious behavioural criteria. Thus, a priori, there was no reason for these two brain regions, which have well-documented roles in auditory and motor processing during vocalizations, to be detected. The role of the midbrain PAG in vocal production is well documented. The PAG is both necessary and sufficient to produce USVs in rodents[7], and lesions in the PAG cause mutism across many species[8,9,50]. We speculate that the expanded OMC-to-PAG projection provides an anatomical substrate for hierarchical motor control of song rhythm. That is, the OMC modulates the song tempo[32,34] (Extended Data Fig. 9), whereas the PAG gates individual notes[50], a finding reminiscent of hierarchical timing circuits in songbirds[51]. Moreover, species with a high ratio of HVC neurons to robust nucleus of the arcopallium neurons, but not the size of the HVC per se, have larger vocal repertoires[52], a result that perhaps reflects convergent circuit solutions to an expansion of vocal capacity in songbirds and rodents. In addition to motor control circuits, vocal communication requires the ability to couple vocal response to auditory input from conspecifics, which depends on auditory circuits[6,11,33]. Closer examination of OMC projections to the AudR (Fig. 2) revealed a spatial overrepresentation in a region ventral to the primary auditory cortex. Moreover, the OMC and AudR seem to be reciprocally connected (Supplementary Fig. 3). This ventral auditory region, which possibly overlaps with the temporal association area, has been shown to be necessary for socially motivated maternal behaviour in laboratory mice[6]. Similar to previous work that has demonstrated a motor to auditory pathway for modulating sensitivity to self-generated sounds[53,54], we speculate that the expanded OMC-to-AudR projection in singing mice might be needed to preserve auditory sensitivity during their own, much louder, vocalizations.

Some limitations should be considered when interpreting these findings. Although MAPseq is a quantitative and scalable tool that can be used to characterize projection patterns at single-cell resolution across many species, the validity of the claims depends on regions that can be reliably identified and dissected on the basis of anatomical markers. Moreover, differences in viral infectivity between species, arising from viral tropism or other causes, must be taken into account during analyses. In this study, these limitations were mitigated by carefully choosing dissection targets and performing additional experiments to confirm synapses in identified targets of interest. Our results point to an exciting central circuit difference between two rodent species, but do not preclude other loci for circuit modifications. Indeed, physical expansion of the ventral pouch in the larynx probably accounts for the lower pitch of singing and pygmy mouse vocalizations compared with the laboratory mouse[55,56] (Fig. 1a). Furthermore, in this study, we did not explored changes that are likely to occur at the genetic, molecular or cellular levels between these two species[57]. Understanding how motor cortical control interfaces with subcortical[7,9,58] as well as peripheral changes[55] will be necessary to fully account for the behavioural divergence. Confirming whether anatomical differences provide a mechanistic basis for behavioural evolution would require additional causal manipulations[50], ideally in multiple intermediate species in the phylogenetic context (Fig. 1a).

Neural circuit differences in adult animals (as reported here) must be established during development[15,59]. Our results provide certain constraints on the developmental mechanisms that might generate this species-specific difference in cortical circuit architecture. Despite the apparent molecular complexity in specifying long-range axonal projections, it seems that a simple wiring rule (binomial model with independence) can explain the majority of motif probabilities. The significantly greater probability of OMC neurons exclusively projecting to the AudR in singing mice is inconsistent with a uniform increase in projection probabilities to all downstream targets. Instead, the selective expansion may occur by direct genetic specification of connectivity strengths in a motif-specific manner. Our result of an expanded direct projection from the OMC to the AudR by reducing collaterals is consistent with the parcellation hypothesis[5]. However, formal testing of the specific mechanisms of long-range connectivity changes (for example,

duplication–divergence) would require the molecular characterization of the OMC with spatial transcriptomics and linking cell types to long-range projection patterns. Such experiments across ontogeny can both uncover developmental mechanisms and test theories of neural circuit evolution.

Large behavioural differences in recently diverged species might be expected to require drastic neural circuit changes. However, recent studies of *Drosophila* spp. have shown that a small number of quantitative changes—in genomes and in central circuits—may be sufficient to produce a large behavioural divergence in closely related species[60–62]. Consistent with this emerging view[16] and building on our previous functional studies[32,34], our results here also suggest that expansion of vocal repertoire in a mammal may not require drastic neural circuit changes (Fig. 2) but may instead proceed by quantitative modifications of preexisting cortical projection motifs (Figs. 3 and 4 and Extended Data Fig. 10). The analytical framework (departure from binomial expectation) described here may even generalize to other model systems for identifying loci of evolutionary change. Taken together, quantitative modifications in ancestral circuit connectivity might be a widespread mechanism for promoting behavioural diversification at short timescales.

Perhaps the most striking example of rapid evolution of a behavioural phenotype is the emergence of human language. Language emerged after our divergence from our closest living relatives, chimpanzees, approximately 6 million years ago[63]. Enhanced cortical control over vocalizations has been proposed to be a key feature of human language[10,11]. We speculate that mechanisms that allow rapid cortex-dependent vocal diversification in rodents might be similar to those required for the evolution of human language in the primate lineage. Genetic mechanisms that underlie morphological innovations (for example, eye structure in animals[64] or prickles in plants[65]) are often conserved over deep evolutionary time, an idea known as deep homology[66]. Similarly, neural mechanisms may also be conserved across a variety of behavioural innovations that require expanded cortical control such as language acquisition. In fact, there is evidence of a strengthened white-matter fibre tract between motor planning and temporal auditory regions in humans compared to chimpanzees and macaques[67]. Elucidating such conserved evolutionary mechanisms is important to understand how neural circuits evolve to create "endless forms most beautiful"[68].

Online content

Any methods, additional references, Nature Portfolio reporting summaries, source data, extended data, supplementary information, acknowledgements, peer review information; details of author contributions and competing interests; and statements of data and code availability are available at https://doi.org/10.1038/s41586-026-10458-y.

1. Geschwind, D. H. & Rakic, P. Cortical evolution: judge the brain by its cover. *Neuron* **80**, 633–647 (2013).
2. Mountcastle, V. The evolution of ideas concerning the function of the neocortex. *Cereb. Cortex* **5**, 289–295 (1995).
3. Krubitzer, L. & Kaas, J. The evolution of the neocortex in mammals: how is phenotypic diversity generated? *Curr. Opin. Neurobiol.* **15**, 444–453 (2005).
4. Chakraborty, M. & Jarvis, E. D. Brain evolution by brain pathway duplication. *Philos. Trans. R. Soc. Lond. B* **370**, 20150056 (2015).
5. Ebbesson, S. O. The parcellation theory and its relation to interspecific variability in brain organization, evolutionary and ontogenetic development, and neuronal plasticity. *Cell Tissue Res.* **213**, 179–212 (1980).
6. Tasaka, G.-I. et al. The temporal association cortex plays a key role in auditory-driven maternal plasticity. *Neuron* **107**, 566–579 (2020).
7. Tschida, K. et al. A specialized neural circuit gates social vocalizations in the mouse. *Neuron* **103**, 459–472 (2019).
8. Jürgens, U. The neural control of vocalization in mammals: a review. *J. Voice* **23**, 1–10 (2009).
9. Schwark, R. W., Fuxjager, M. J. & Schmidt, M. F. Proposing a neural framework for the evolution of elaborate courtship displays. *eLife* https://doi.org/10.7554/eLife.74860 (2022).
10. Simonyan, K. & Horwitz, B. Laryngeal motor cortex and control of speech in humans. *Neuroscientist* **17**, 197–208 (2011).
11. Castellucci, G. A., Kovach, C. K., Howard, M. A. III, Greenlee, J. D. W. & Long, M. A. A speech planning network for interactive language use. *Nature* **602**, 117–122 (2022).
12. Striedter, G. F. *Principles of Brain Evolution* (Sinauer Associates, 2005).
13. Lindhout, F. W., Krienen, F. M., Pollard, K. S. & Lancaster, M. A. A molecular and cellular perspective on human brain evolution and tempo. *Nature* **630**, 596–608 (2024).
14. Barker, A. J. Brains and speciation: control of behavior. *Curr. Opin. Neurobiol.* **71**, 158–163 (2021).
15. Tosches, M. A. Developmental and genetic mechanisms of neural circuit evolution. *Dev. Biol.* **431**, 16–25 (2017).
16. Roberts, R. J. V., Pop, S. & Prieto-Godino, L. L. Evolution of central neural circuits: state of the art and perspectives. *Nat. Rev. Neurosci.* **23**, 725–743 (2022).
17. Sakurai, A. & Katz, P. S. Command or obey? Homologous neurons differ in hierarchical position for the generation of homologous behaviors. *J. Neurosci.* **39**, 6460–6471 (2019).
18. Jorstad, N. L. et al. Comparative transcriptomics reveals human-specific cortical features. *Science* https://doi.org/10.1126/science.ade9516 (2023).
19. Barton, R. A. & Harvey, P. H. Mosaic evolution of brain structure in mammals. *Nature* **405**, 1055–1058 (2000).
20. Bianchi, S. et al. Dendritic morphology of pyramidal neurons in the chimpanzee neocortex: regional specializations and comparison to humans. *Cereb. Cortex* **23**, 2429–2436 (2013).
21. Krienen, F. M. et al. Innovations present in the primate interneuron repertoire. *Nature* **586**, 262–269 (2020).
22. Kebschull, J. M. et al. Cerebellar nuclei evolved by repeatedly duplicating a conserved cell-type set. *Science* https://doi.org/10.1126/science.abd5059 (2020).
23. Gu, Z. et al. Control of species-dependent cortico-motoneuronal connections underlying manual dexterity. *Science* **357**, 400–404 (2017).
24. Dum, R. P. & Strick, P. L. The origin of corticospinal projections from the premotor areas in the frontal lobe. *J. Neurosci.* **11**, 667–689 (1991).
25. Winding, M. et al. The connectome of an insect brain. *Science* **379**, eadd9330 (2023).
26. White, J. G., Southgate, E., Thomson, J. N. & Brenner, S. The structure of the nervous system of the nematode *Caenorhabditis elegans*. *Philos. Trans. R. Soc. Lond. B* **314**, 1–340 (1986).
27. The MICrONS Consortium. Functional connectomics spanning multiple areas of mouse visual cortex. *Nature* **640**, 435–447 (2025).
28. Banerjee, A., Phelps, S. M. & Long, M. A. Singing mice. *Curr. Biol.* **29**, R190–R191 (2019).
29. Hooper, E. T. & Carleton, M. D. *Reproduction, Growth and Development in Two Contiguously Allopatric Rodent Species, Genus Scotinomys* Miscellaneous Publications No. 151 (Univ. of Michigan, 1976).
30. Miller, J. R. & Engstrom, M. D. Vocal stereotypy and singing behavior in baiomyine mice. *J. Mammal.* **88**, 1447–1465 (2007).
31. Pasch, B., Bolker, B. M. & Phelps, S. M. Interspecific dominance via vocal interactions mediates altitudinal zonation in neotropical singing mice. *Am. Nat* **182**, E161–E173 (2013).
32. Okobi, D. E. Jr, Banerjee, A., Matheson, A. M. M., Phelps, S. M. & Long, M. A. Motor cortical control of vocal interaction in neotropical singing mice. *Science* **363**, 983–988 (2019).
33. Banerjee, A. & Vallentin, D. Convergent behavioral strategies and neural computations during vocal turn-taking across diverse species. *Curr. Opin. Neurobiol.* **73**, 102529 (2022).
34. Banerjee, A., Chen, F., Druckmann, S. & Long, M. A. Temporal scaling of motor cortical dynamics reveals hierarchical control of vocal production. *Nat. Neurosci.* **27**, 527–535 (2024).
35. Mercer Lindsay, N. et al. Orofacial movements involve parallel corticobulbar projections from motor cortex to trigeminal premotor nuclei. *Neuron* **104**, 765–780 (2019).
36. Komiyama, T. et al. Learning-related fine-scale specificity imaged in motor cortex circuits of behaving mice. *Nature* **464**, 1182–1186 (2010).
37. Steppan, S. J. & Schenk, J. J. Muroid rodent phylogenetics: 900-species tree reveals increasing diversification rates. *PLoS ONE* **12**, e0183070 (2017).
38. Floody, O. R. in *Handbook of Ultrasonic Vocalization—A Window into the Emotional Brain* (ed. Brudzynski, S. M.) 197–206 (Elsevier, 2018).
39. Kalcounis-Rueppell, M. C., Metheny, J. D. & Vonhof, M. J. Production of ultrasonic vocalizations by *Peromyscus* mice in the wild. *Front. Zool.* **3**, 3 (2006).
40. Fujishima, Y. & Long, M. A. Advertisement vocalizations support home-range defense in the singing mouse. *Curr. Biol.* **35**, 2960–2966 (2025).
41. Muñoz-Castañeda, R. et al. Cellular anatomy of the mouse primary motor cortex. *Nature* **598**, 159–166 (2021).
42. Vargas, C. D. M. et al. A functional and non-homuncular representation of the larynx in the primary motor cortex of mice, a vocal non-learner. Preprint at *bioRxiv* https://doi.org/10.1101/2024.02.05.579004 (2024).
43. Kebschull, J. M. et al. High-throughput mapping of single-neuron projections by sequencing of barcoded RNA. *Neuron* **91**, 975–987 (2016).
44. Han, Y. et al. The logic of single-cell projections from visual cortex. *Nature* **556**, 51–56 (2018).
45. Tripp, J. A. & Phelps, S. M. Females counter-sing, but response to male song differs by sex in Alston's singing mouse. *Biol. Lett.* **20**, 20230484 (2024).
46. Pasch, B., George, A. S., Hamlin, H. J., Guillette, L. J. Jr & Phelps, S. M. Androgens modulate song effort and aggression in neotropical singing mice. *Horm. Behav.* **59**, 90–97 (2011).
47. Hage, S. R. & Nieder, A. Dual neural network model for the evolution of speech and language. *Trends Neurosci.* **39**, 813–829 (2016).
48. Tyssowski, K. M. et al. Evolutionary expansion of the corticospinal system is linked to dexterity in *Peromyscus* mice. Preprint at *bioRxiv* https://doi.org/10.1101/2025.10.16.682851 (2025).
49. Jourjine, N. & Hoekstra, H. E. Expanding evolutionary neuroscience: insights from comparing variation in behavior. *Neuron* **109**, 1084–1099 (2021).
50. Zheng, X. M., Harpole, C. E., Davis, M. B. & Banerjee, A. Vocal repertoire expansion in singing mice by co-opting a conserved midbrain circuit node. *Curr. Biol.* **35**, 5762–5778 (2025).
51. Fee, M. S. & Scharff, C. The songbird as a model for the generation and learning of complex sequential behaviors. *ILAR J.* **51**, 362–377 (2010).
52. Moore, J. M. & DeVoogd, T. J. Concerted and mosaic evolution of functional modules in songbird brains. *Proc. Biol. Sci.* https://doi.org/10.1098/rspb.2017.0469 (2017).

53. Harmon, T. C., Madlon-Kay, S., Pearson, J. & Mooney, R. Vocalization modulates the mouse auditory cortex even in the absence of hearing. *Cell Rep.* **43**, 114611 (2024).
54. Schneider, D. M., Sundararajan, J. & Mooney, R. A cortical filter that learns to suppress the acoustic consequences of movement. *Nature* **561**, 391–395 (2018).
55. Smith, S. K., Burkhard, T. T. & Phelps, S. M. A comparative characterization of laryngeal anatomy in the singing mouse. *J. Anat.* **238**, 308–320 (2021).
56. Riede, T. & Pasch, B. Pygmy mouse songs reveal anatomical innovations underlying acoustic signal elaboration in rodents. *J. Exp. Biol.* **223**, jeb223925 (2020).
57. Bendesky, A. et al. The genetic basis of parental care evolution in monogamous mice. *Nature* **544**, 434–439 (2017).
58. Sweeney, L. B. & Kelley, D. B. Harnessing vocal patterns for social communication. *Curr. Opin. Neurobiol.* **28**, 34–41 (2014).
59. Hoke, K. L., Adkins-Regan, E., Bass, A. H., McCune, A. R. & Wolfner, M. F. Co-opting evo-devo concepts for new insights into mechanisms of behavioural diversity. *J. Exp. Biol.* **222**, jeb190058 (2019).
60. Ding, Y. et al. Neural evolution of context-dependent fly song. *Curr. Biol.* **29**, 1089–1099 (2019).
61. Seeholzer, L. F., Seppo, M., Stern, D. L. & Ruta, V. Evolution of a central neural circuit underlies *Drosophila* mate preferences. *Nature* **559**, 564–569 (2018).
62. Auer, T. O. et al. Olfactory receptor and circuit evolution promote host specialization. *Nature* **579**, 402–408 (2020).
63. Fitch, W. T. The evolution of speech: a comparative review. *Trends Cogn. Sci.* **4**, 258–267 (2000).
64. von Salvini-Plawen, L. & Mayr, E. in *Evolutionary Biology* (eds Hecht, M. K. et al.) 207–263 (Springer, 1977).
65. Satterlee, J. W. et al. Convergent evolution of plant prickles by repeated gene co-option over deep time. *Science* **385**, eado1663 (2024).
66. Shubin, N., Tabin, C. & Carroll, S. Deep homology and the origins of evolutionary novelty. *Nature* **457**, 818–823 (2009).
67. Balezeau, F. et al. Primate auditory prototype in the evolution of the arcuate fasciculus. *Nat. Neurosci.* **23**, 611–614 (2020).
68. Darwin, C. *On the Origin of Species* (John Murray, 1859).

Methods

Mouse husbandry

All experiments were approved and conducted in accordance with the Cold Spring Harbor Laboratory Institutional Animal Care and Use Committee. All animals used were adult (>3 months) male and female mice. Laboratory mice were acquired from The Jackson Laboratory (C57BL/6J). Colonies of laboratory and singing mice were maintained at 20–22 °C, 30–70% humidity and a 12–12 h light–dark cycle.

Behavioural recordings and analysis

A female of each species was muted by synaptic silencing of the caudolateral PAG using tetanus-toxin light chain[7,50] and allowed 2 weeks for protein expression. For five sessions per species, the mute female was placed with a conspecific male in a clean cage for interaction (Thoren Systems 8; 30.8 × 40.6 × 22.2 cm) lined with Alpha-pad cotton paper (Shepherd Specialty Papers). Audio of each dyad was recorded for 1–2 h using two Avisoft CM16/CMPA microphones positioned above the cage with high and low gain settings and sampling at 250 kHz (digitized with Avisoft UltraSoundGate 116H). Vocalizations were segmented from the audio using USVSEG[69] software for MATLAB (v.09r2), and parameters were optimized to the sounds emitted by each species. For singing mice, songs and their individual notes were also detected using custom code in Python. Segmented sounds were manually curated in a customized spectrogram browser derived from the open-source MATLAB graphical user interface DeepSqueak[70]. Curation consisted of correcting any vocalization boundary errors and removal of abiotic false positives. Spectrogram inspection confirmed that stimulus females were mute, with no overlapping vocalizations observed; female singing mice also ceased singing during continuous post-surgery monitoring. Songs were operationally defined as sequences of loud notes with a minimum duration of 1.5 s and gaps of no greater than 0.5 s. Song notes were defined as part of the songs, whereas the remaining quiet notes were classified as USVs[50]. For each curated note, we calculated the maximum amplitude in a fixed frequency range (10–100 kHz). We calculated the instantaneous note rate as the inverse of the interval between two consecutive note start times. For note pitch, the minimum of the fundamental frequency of each note was calculated in Python, using USVSEG-based preprocessing to enhance vocal signals and to suppress background noise[69]. Kernel densities for note acoustic parameters were calculated using the kdeplot function in the Python package seaborn[71], specifying either two or five levels.

Stereotaxic viral injections

Before surgery, subcutaneous meloxicam was delivered at a dose of 2 mg kg^{-1}. Surgeries were performed on a stereotaxic apparatus under 1–2% isoflurane in oxygen. The OMC was localized on the basis of published data (laboratory mice, refs. 35,36; singing mice, ref. 32), which identifies the OMC as the area in the motor cortex that, when stimulated, results in orofacial muscle contraction (coordinates relative to bregma: anterior–posterior (AP), 2.25 mm; medial–lateral (ML), 2.25 mm). These coordinates were used for all OMC injections unless otherwise noted. To mute female stimulus mice for behavioural recordings, we bilaterally expressed tetanus-toxin light chain[7,50] in the caudolateral PAG using AAVs. A female singing mouse and a laboratory mouse were bilaterally injected in the caudolateral PAG with 80 nl of a 1:1 mixture of AAV2/DJ-hSyn-flex-TeLC-eYFP (custom packaged by WZ Biosciences) and CamKII-Cre. The following coordinates were used: singing mouse, AP, −4.2 mm; ML: ±0.6 mm; dorsal–ventral (DV), −2.3 mm (ref. 50); laboratory mouse, AP, −4.7 mm; ML, ±0.7 mm; DV, −1.75 (ref. 7).

Histology of these mice were also used in anterograde trans-synaptic tracing of the OMC to the PAG.

For mapping of bulk neuronal projections, neurons were targeted to express tdTomato using a 1:1 mixture of CaMKII-Cre and FLEX-tdTomato viruses (Supplementary Table 1). Next, 30 nl of this viral mixture was injected into the OMC at two depths: 500 and 750 µm ventral to the brain surface.

For MAPseq viral injections, Sindbis virus carrying the barcode library[72] was diluted 1:3 in sterile saline. The OMC was injected with 50 nl of diluted Sindbis virus at 300, 600 and 900 µm ventral to the brain surface at two locations: AP, 2.0 and 2.5 mm; and ML, 2.25 mm.

For visualizing synaptic boutons, a 1:1 mixture of CaMKII-Cre and Flex-mGFP-2A-Synaptophysin-mRuby (Supplementary Table 1) was injected into the OMC using the coordinates listed above. Specifically, 60 nl of this viral mixture was injected at two depths: 500 and 750 µm ventral to the brain surface.

For anterograde trans-synaptic tracing[73] of the OMC to the AudR, a 1:1 mixture of CaMKII-Cre and DIO-mCherry (Supplementary Table 1) was injected into the OMC of singing mice. Specifically, 80 nl was injected at depths of 500 and 750 µm ventral to the brain surface. DIO-eGFP virus (Supplementary Table 1) was injected into the AudR (AP, −1.2; ML, 4.25 mm). Three injections of 50 nl at 2-min intervals were delivered at a single depth of 2.3 mm ventral to the brain surface.

For retrograde tracing of the OMC, retrograde AAV carrying either GFP or GFP-NLS (Supplementary Table 1) was injected into the OMC of laboratory or singing mice. Next, 30 nl of virus was injected at two depths: 500 and 750 µm ventral to the brain surface.

Mice were transcardially perfused with 4 °C PBS and then with 4 °C 4% paraformaldehyde (PFA) 14 days after injection for OMC projection mapping, 44 h after injection for MAPseq experiment or 21 days after injection for all other viral tracing experiments.

Confocal imaging

After transcardial perfusion, brains were fixed in 4% PFA at 4 °C for 24 h. Brains were rinsed with PBS then embedded in 3% agarose. Brains were sectioned on a vibratome at 50 µm, stained with DAPI and mounted on glass slides with ProLong Gold Antifade mountant. Microscopy images were acquired in Airyscan SR-4Y multiplexing mode using a Zeiss LSM 980 Airyscan2 inverted confocal laser scanning microscope (Carl Zeiss Microscopy), equipped with a Plan-Apochromat ×10/0.45 NA M27 air-objective lens. DAPI was excited using a 405 nm diode laser, mCherry and tdTomato fluorophores were excited with a 561 nm diode laser, and GFP and YFP fluorophores were excited with a 488 nm diode laser. Emission signals for fluorophore signals were collected using a 32-channel gallium arsenide phosphide (GaAsP-PMT) Airyscan detector, operated in frame scanning mode with a pixel dwell time of 0.51 µs. Airyscan raw images were processed in Zeiss ZEN Blue (v.3.8.2) software using Fast Airyscan SheppardSum SR-4Y processing with an automated 2D Weiner filter (standard strength).

STPT imaging and image processing

STPT imaging was conducted using established protocols[74,75]. First, brains were embedded in 4% oxidized agarose followed by crosslinking in 0.2% sodium borohydrate solution. To image tdTomato projections from the OMC in the whole brain, entire coronal planes of the embedded brains were imaged every 50 µm on a TissueCyte 1000 STPT microscope (Tissuevision) by tiling and slicing the brain. A chameleon ultra (coherent) 150 fs pulsed laser at 930 nm, Olympus objective (×20, NA = 1.0) and 602/70 emission filter were used to image at 1 µm per pixel lateral resolution. Image correction and stitching was completed using custom-built software[74,75].

STPT data analysis

Alignment of image stacks to Allen CCF. Twenty-fold scaled down images were used for comprehensive and easy visualization between brains. Brains from a representative laboratory mouse and a singing mouse were chosen as a reference to align brains in the species. The Allen Brain atlas (2022 CCFv3)[76] was also registered to each brain using the brainreg function with default parameters from the brainglobe suite (https://brainglobe.info/index.html)[77]. Annotated areas from

the aligned Allen brain atlas were used to determine volumes of major brain regions. To determine the injection site of each animal, a threshold was determined using Otsu's method. The intersection of the combined annotated primary and secondary motor cortical regions and the thresholded data were used to create a mask of the injection site for each brain. Injection sites of aligned brains were maximum projected in the DV axis to determine overlap between brains.

Quantification of fluorescent axonal signal. High-resolution images were visualized in Napari (v.0.5.6)[77]. Target regions of interest (OMCc, AudR, PAG and SNr) were then manually outlined using the Napari plugin brainglobe-segmentation[78]. Digital dissections were guided by anatomical landmarks to match MAPseq dissections as closely as possible. The injection site (OMCi) of each animal was outlined based on the presence of fluorescent cell bodies. Outlines were used to create a mask and applied to each relevant brain region. Images were then imported into LABKIT[79], which was used to train a classifier to segment axonal fluorescent signals from background (Extended Data Fig. 6a,b). The classifier was trained on a representative image from every region in every mouse. After applying the trained classifier to all images, the segmented volume of each region was calculated and normalized to the injection site volume in each animal (Extended Data Fig. 6d). The fold change was calculated by taking the average normalized volume of each region among laboratory or singing mice (Extended Data Fig. 6e).

MAPseq tissue processing

After transcardial perfusion, brains were fixed in 4% PFA at 4 °C for 24 h. The brains were then rinsed with PBS and transferred to 300 mM glycine for 24 h at 4 °C. After incubation, brains were embedded in cryoembedding medium and frozen for sectioning. Brains were cut coronally at 200–250 µm sections for microdissection. Injection sites were identified through bright-field imaging of GFP. Target regions were chosen to include all OMC projection targets based on our STPT data, and regional boundaries were identified through visual landmarks determined from the Allen brain atlas as well as our STPT data (Supplementary Figs. 1 and 2). During dissection, samples were kept on wet ice during dissection. Throughout the procedure, tools and blades were changed between dissection targets and gloves were changed between samples to prevent area and sample cross-contamination. Samples were collected from the olfactory bulb and hippocampus as negative controls. Barcode RNA was extracted, reverse-transcribed and amplified using a published protocol[43,80]. An Illumina sequencing library was generated and sequenced on an Illumina NextSeq500 sequencer. Possible artefacts, including the effect of fibres of passage, viral toxicity, co-infections, double use of a single barcode sequence and various other sources of false negatives and false positives, have been previously characterized[43,44]. Notably, although MAPseq, like GFP tracing, does not distinguish fibres of passage, their contribution is minimized by avoiding large fibre bundles during the dissection of target areas. Also, by specifically injecting the barcodes into the OMC and subsequently only sequencing the barcode RNA, we only obtained signals from the targeted OMC neurons. Therefore, our results will not be affected by other non-OMC-projecting neurons to the target regions.

MAPseq data analysis

After sequencing, reads were demultiplexed, and the absolute counts of each barcode were determined on the basis of the unique molecular identifier sequence and error-corrected barcode sequences matched to the sequenced virus library. A matrix of size ((number of barcodes) × (number of dissected areas)) was constructed, whereby matrix entries corresponded to the absolute counts of individual barcodes in each area. Only barcodes with at least 30 barcode molecules at the injection site and 5 barcode molecules at the maximum target site were used. A barcode was determined to project to a target site if there were at least four barcode molecules at that target site. This threshold minimized barcode detection in negative control target regions. We did not find significant differences in OMC projections to the anterior or posterior PAG in either species (Wilcoxon signed-rank test, $P > 0.05$). Therefore, we decided to pool all barcodes to the PAG.

Heatmaps and cell-type labelling. Normalized barcode counts were calculated from barcode counts normalized to a RNA spike-in of known concentration and quantity in each sample. For heatmaps, 1,000 unique barcodes (that is, neurons) were randomly sampled from an individual laboratory or singing mouse, and the normalized barcode counts were plotted (Fig. 3b) and used to compare Sindbis infectivity between species (Extended Data Fig. 4a,b). Neurons were classified into three major projection, excitatory cell types: IT, CT and PT. PT cells were first defined as neurons having any projection to a midbrain or hindbrain region (HY, PG, PAG, SNr, SCm or HB). CT cells were defined as having no projections to midbrain or hindbrain regions, but having a projection to the thalamus. IT cells were defined as cells having no projections to the midbrain, hindbrain or thalamic regions, and only projections to the striatum and/or cortex.

Modelling extent of innervation. To eliminate animal-to-animal batch effects, we calculated a normalized barcode expression value. For each animal, we took the normalized barcode counts and divided these counts by the mean normalized barcode count at the injection site (OMCi). The normalized barcode expression was taken as a proxy for the amount of axonal material in each dissected area. The empirical cumulative distribution function of the normalized barcode expression for all neurons in a region was plotted to compare species differences. The median value of normalized expression in each region for an individual animal was compared between species, and a two-sided Mann–Whitney *U*-test was performed to determine species differences.

Modelling projection probabilities. To calculate the proportion of neurons projecting to different target regions, the data were binarized (threshold of four barcode counts). Proportions were calculated for each major cell type. This approach accounts for any potential variance in the infectivity across cortical layers, which could bias the relative proportion of major cell types in the dataset. For example, the proportion of OMC neurons projecting to the AudR regions were the number of unique barcodes that had above the threshold signal (at least four barcode counts) in the AudR region divided by the total number of unique barcodes classified as IT cells. AudR, OMCc and STR proportions were calculated over the total IT population. HY, PG, PAG, SNr, SCm and HB proportions were calculated over the PT population. A two-sided Mann–Whitney *U*-test was used to calculate significant differences between individuals of each species on a per area basis.

Degree and motif analyses. The node degree for a given neuron was defined as the number of projecting areas each neuron has. For instance, if a neuron has projections in the AudR and STR, this neuron would have a node degree of 2. For degree and motif analyses, only IT cells were analysed as there were many fewer PT cells per degree and motif. Motif proportions were calculated for IT cells of an individual mouse. The motif proportions were calculated on the basis of an estimation of the total IT cell population as previously derived[44]. In brief, the total IT cell population was adjusted to account for unobserved neurons with projections to uncollected regions or without projections. The total IT cell population can be estimated on the basis of finding the roots of a polynomial derived from observed numbers of neurons to collected regions. The total IT population was calculated for each individual mouse and used as the denominator for determining the observed proportion for each motif. The expected proportion for each motif was calculated by multiplying the probabilities of projecting to individual brain regions according to a binomial model. The difference between the experimentally observed versus expected proportions for each

motif was aggregated for every individual animal. *P* values were calculated under the binomial model for each individual singing mouse, and the Fisher's method was used to combine *P* values across individuals. The extent of deviation from the binomial model was computed for each species, and their distributions were compared using an *F*-test for equality of two variances.

Calculating total OMC neuron population. In our MAPseq experiment, the number of IT neurons was defined as the number of neurons that project exclusively to IT regions; that is, neurons that project to the AudR, OMCc and/or STR. However, the observed number of IT neurons in a MAPseq dataset is a biased sampling of OMC neurons. Owing to the nature of the technique, we did not account for neurons that could be part of the OMC IT population but project to regions outside the regions we sampled. Therefore, the number of OMC IT neurons we counted in our dataset is an underestimate of the total OMC IT population. If we wanted to make reasonable motif predictions under a binomial model, the total OMC IT population count must be adjusted. As previously described[44], we can derive an estimate for the total OMC IT neurons (N_{total}) for each individual animal using our observed counts of how many neurons project to each target region. First, we observe that:

$$Prob_{\text{neuron projects to at least one region}} + Prob_{\text{neuron projects to no regions}} = 1. \quad (1)$$

We can also assume that the proportion of neurons that projects to a region is equivalent to the probability that a neuron projects to that region:

$$Prob_{\text{region}} = \frac{N_{\text{region}}}{N_{\text{total}}} \quad (2)$$

where N_{region} is the number of neurons that project to that region, and N_{total} is the total number of OMC IT neurons. Considering we have three IT target regions (OMCc, AudR and STR), we can combine the above two equations to obtain the following equation:

$$\left(\frac{N_{\text{obs}}}{N_{\text{total}}}\right) + \left(\left(1 - \frac{N_{\text{OMCc}}}{N_{\text{total}}}\right)\left(1 - \frac{N_{\text{AudR}}}{N_{\text{total}}}\right)\left(1 - \frac{N_{\text{STR}}}{N_{\text{total}}}\right)\right) = 1 \quad (3)$$

where N_{obs} is the number of unique barcodes (neurons) we recovered in our MAPseq experiment, N_{OMCc}, N_{STR} and N_{AudR} are the numbers of unique barcodes found to project to each individual area (OMCc, STR or AudR), and N_{total} is the total number of IT neurons that we are trying to account for. Expanding and rearranging the above equation, we can derive the following quadratic equation:

$$\begin{aligned}(N_{\text{obs}} - N_{\text{OMCc}} - N_{\text{AudR}} - N_{\text{STR}})N_{\text{total}}^2 + (N_{\text{OMCc}}N_{\text{AudR}} \\ + N_{\text{OMCc}}N_{\text{STR}} + N_{\text{AudR}}N_{\text{STR}})N_{\text{total}} - (N_{\text{OMCc}}N_{\text{AudR}}N_{\text{STR}}) = 0.\end{aligned} \quad (4)$$

We can then use a roots solver to solve for N_{total}. For each animal, we used the observed barcode counts for each region and calculated a quadratic equation using the above formula. We then used a roots solver to find the largest real root. We used this number as the adjusted OMC IT population size (N_{total}) and used this N_{total} to calculate the probability that a neuron projects to an individual region. We used these adjusted probabilities to estimate motif proportions expected under the binomial model to provide us with more accurate predictions.

Bootstrap resampling to match the number of neurons across species. Because more unique barcodes were recovered for laboratory mice, we verified our findings by matching the number of neurons in singing mice with a downsampled population of neurons in the laboratory mice. First, all laboratory mouse neurons of the same cell type (IT or PT) were pooled. The pooled neurons were randomly sampled, without replacement, seven times to exactly match the number of neurons recovered in each of the singing mice. Downstream target proportions and IT motif proportions were calculated for this downsampled population of laboratory mouse neurons. A two-sided Mann–Whitney *U*-test was used to calculate IT motif proportion differences between species.

Analysis of OMC cooling data

We analysed a previously published OMC cooling dataset[32] to assess the causal contribution of the OMC on song rhythm. The instantaneous note rate was defined as the reciprocal of the time between successive note onsets. For each note, the instantaneous note rate was plotted against the time since the song start to construct song trajectories. For each animal, the difference between the instantaneous note rates for cooled and uncooled songs was calculated for all notes within each second (that is, a bin size of 1 s). Means and error bars (corresponding to s.e.m.) were calculated across all nine animals. Significance was evaluated with a two-sample *t*-test.

Reporting summary

Further information on research design is available in the Nature Portfolio Reporting Summary linked to this article.

Data availability

The data used in this study can be downloaded from Dryad (https://doi.org/10.5061/dryad.8kprr4z2p)[81]. Additional inquiries or requests will be fulfilled by the lead authors.

Code availability

The code for analysing data is freely available on GitHub (https://github.com/singingmicelab/Isko-2026-MAPseq-code.git).

69. Tachibana, R. O., Kanno, K., Okabe, S., Kobayasi, K. I. & Okanoya, K. USVSEG: a robust method for segmentation of ultrasonic vocalizations in rodents. *PLoS ONE* **15**, e0228907 (2020).
70. Coffey, K. R., Marx, R. E. & Neumaier, J. F. DeepSqueak: a deep learning-based system for detection and analysis of ultrasonic vocalizations. *Neuropsychopharmacology* **44**, 859–868 (2019).
71. Waskom, M. L. seaborn: statistical data visualization. *J. Open Source Softw.* https://doi.org/10.21105/joss.03021 (2021).
72. Yuan, L., Chen, X., Zhan, H., Henry, G. L. & Zador, A. M. Massive multiplexing of spatially resolved single neuron projections with axonal BARseq. *Nat. Commun.* **15**, 8371 (2024).
73. Zingg, B. et al. AAV-mediated anterograde transsynaptic tagging: mapping corticocollicular input-defined neural pathways for defense behaviors. *Neuron* **93**, 33–47 (2017).
74. Ragan, T. et al. Serial two-photon tomography for automated ex vivo mouse brain imaging. *Nat. Methods* **9**, 255–258 (2012).
75. Kim, Y. et al. Brain-wide maps reveal stereotyped cell-type-based cortical architecture and subcortical sexual dimorphism. *Cell* **171**, 456–469 (2017).
76. Wang, Q. et al. The Allen Mouse Brain Common Coordinate Framework: a 3D reference atlas. *Cell* **181**, 936–953 (2020).
77. Napari Contributors. *napari: A Multi-Dimensional Image Viewer for Python* (Napari, 2019).
78. Tyson, A. L. et al. Accurate determination of marker location within whole-brain microscopy images. *Sci. Rep.* **12**, 867 (2022).
79. Arzt, M. et al. LABKIT: Labeling and segmentation toolkit for big image data. *Front. Comput. Sci.* **4**, 777728 (2022).
80. Zhan, H., Kebschull, J. & Zador, A. M. MAPseq (multiplexed analysis of projections by sequencing) sample processing protocol. *protocols.io* https://doi.org/10.17504/protocols.io.bsm9nc96 (2021).
81. Isko, E. et al. Data from: Specific expansion of motor cortical projections in a singing mouse. *Dryad* https://doi.org/10.5061/dryad.8kprr4z2p (2026).

Acknowledgements We thank J. Kebschull, J. Tollkuhn, G. Castellucci, M. Long, S. Ghosh and members of the Banerjee and Zador Laboratories for comments on earlier versions of this manuscript; A. Williams, R. Drewes, T. Genovese, S. Kaushalya and staff at the MAPseq core facility, including Y. Wu, D. Ravens and C. Freivald, for their technical assistance. Confocal microscopy was performed with assistance from the CSHL Microscopy Shared Resource, which is supported by Cancer Center Support grant 5P30CA045508 and by NIH Award 1S10OD034372-01 to purchase the Zeiss LSM 980 with Airyscan2. This work was also funded by NIH BRAIN initiative grant 1RF1NS132046-01 (to A.B.), the Searle Scholars Program (to A.B.), the Esther A. & Joseph Klingenstein Fund (to A.B.), a McKnight Scholars Award (to A.B.), a Konishi Neuroethology Award (to C.E.H.), and NSF–GRFP 1938105 (to E.C.I.).

Author contributions A.B. and A.M.Z. conceptualized and supervised the project. C.E.H. and X.M.Z. collected the behavioural data. E.C.I., C.E.H. and M.B.D. generated viral tracing data, and E.C.I. and C.E.H. collected the STPT imaging data. E.C.I. generated MAPseq data with help from H.Z. for tissue processing. Formal analysis was conducted by E.C.I. Visualization of data was done by E.C.I. and A.B. The original manuscript draft was written by E.C.I. and A.B. then edited and reviewed by E.C.I., A.B. and A.M.Z.

Competing interests The authors declare no competing interests.

Additional information

Supplementary information The online version contains supplementary material available at https://doi.org/10.1038/s41586-026-10458-y.

Correspondence and requests for materials should be addressed to Anthony M. Zador or Arkarup Banerjee.

Peer review information *Nature* thanks the anonymous reviewers for their contribution to the peer review of this work. Peer reviewer reports are available.

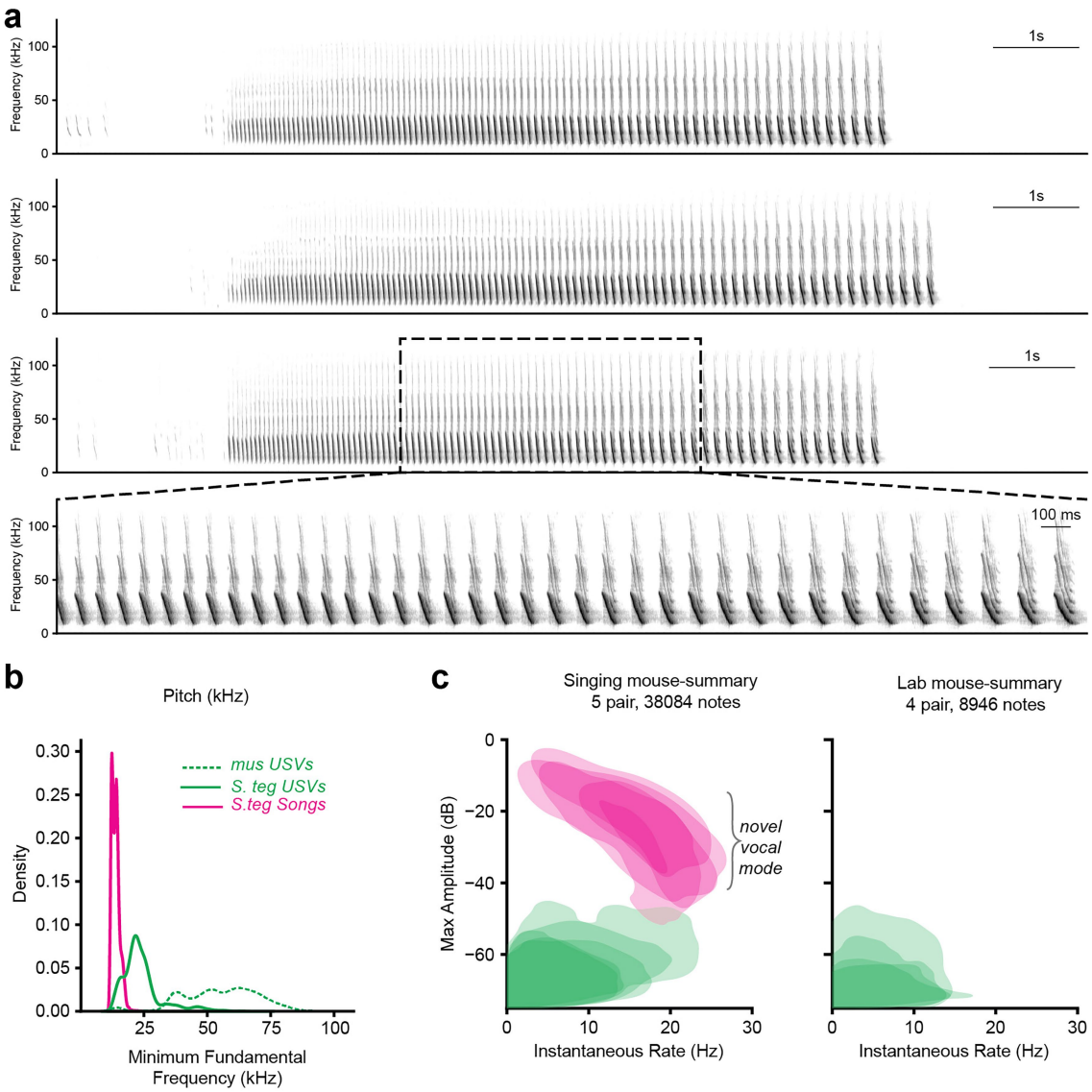

Extended Data Fig. 1 | Analysis of vocal features. (**a**) Three example songs that are composed of a series of frequency-modulated down-sweeps that progress stereotypically over many seconds. Zoomed portion of a song (*bottom*) shows that individual notes are shorter in the beginning and progressively increase in duration as the song progresses. (**b**) Lowest fundamental pitch of notes for singing mouse song (*solid, magenta line*), singing mouse USV (*solid, green line*), and lab mouse USV (*dashed, green line*). (**c**) Same data as plotted in **1e**, but each shaded area is the kernel density estimate for a individual mouse.

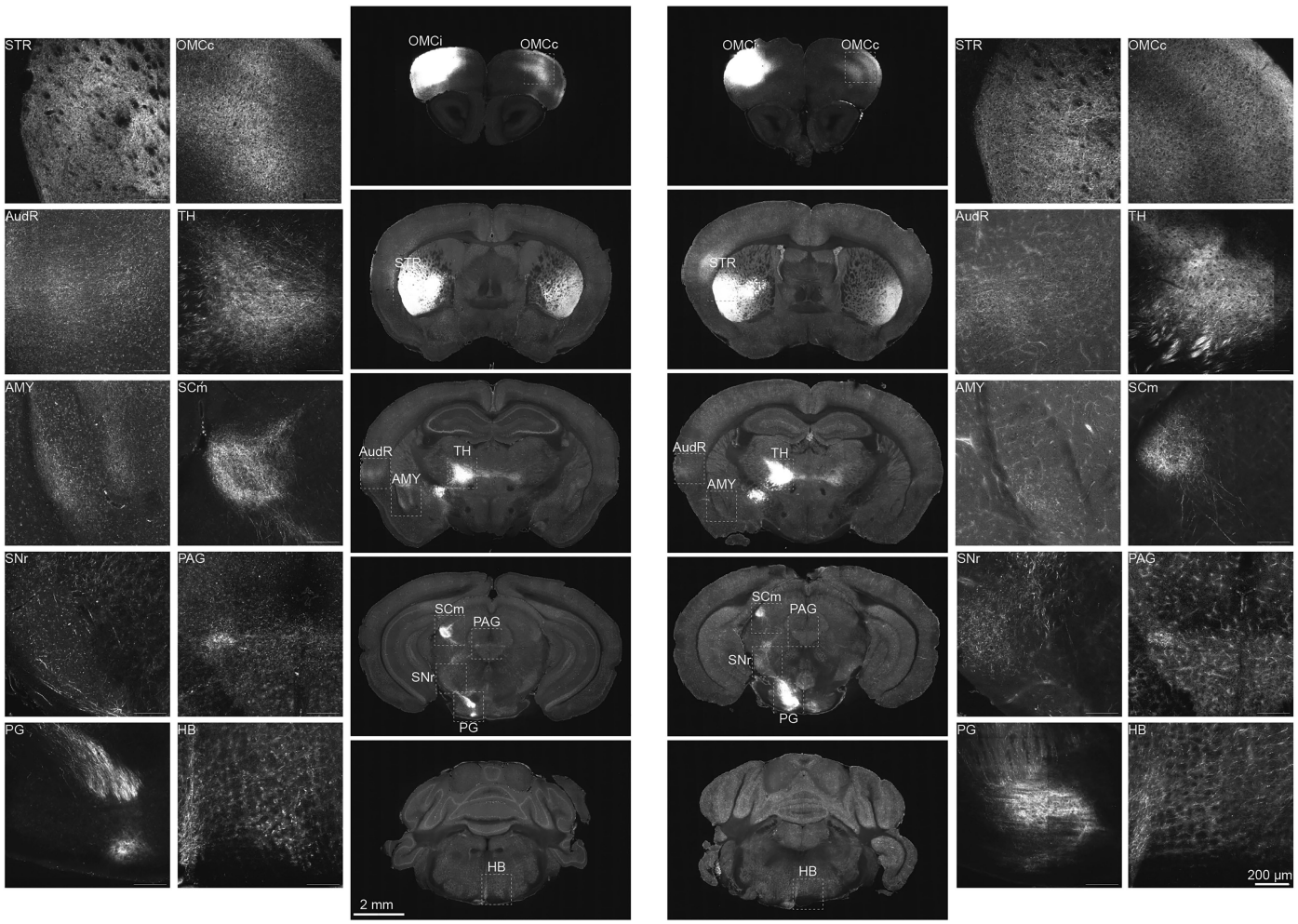

Extended Data Fig. 2 | Two-photon microscopy images of OMC projections to target regions in lab and singing mice. Regions displayed were chosen as MAPseq dissection target regions due to the presence of OMC axonal projections. Abbreviations: Orofacial motor cortex ipsilateral (OMCi), orofacial motor cortex contralateral (OMCc), striatum (STR), thalamus (TH), auditory region (AudR), amygdala (AMY), superior colliculus motor (SCm), substantia nigra (SNr), periaqueductal gray (PAG), pontine gray (PG), hindbrain (HB). These patterns of axonal projections were replicable across the 3 lab and 3 singing mice imaged.

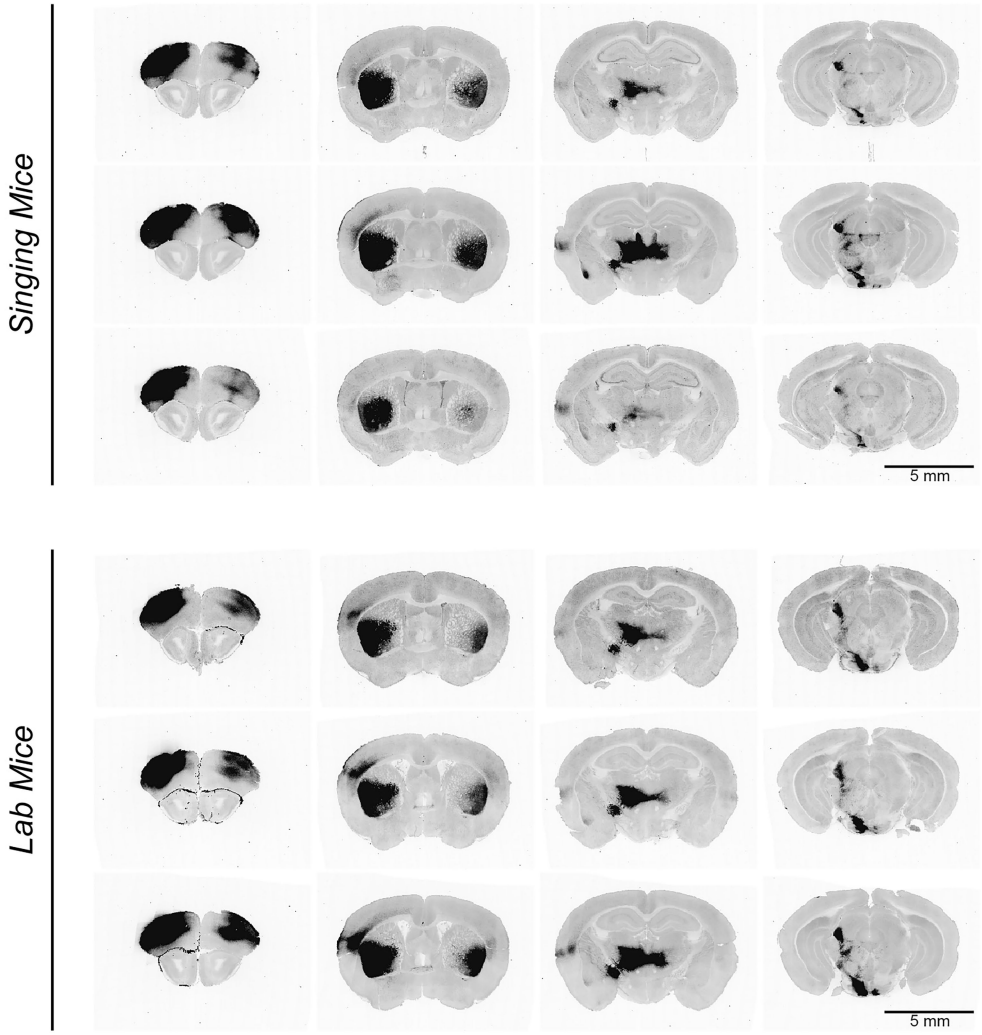

Extended Data Fig. 3 | Bulk OMC projections in singing and lab mice across replicates. Representative coronal slices along the rostrocaudal axis (left to right) in individual animals (n = 3) from both species.

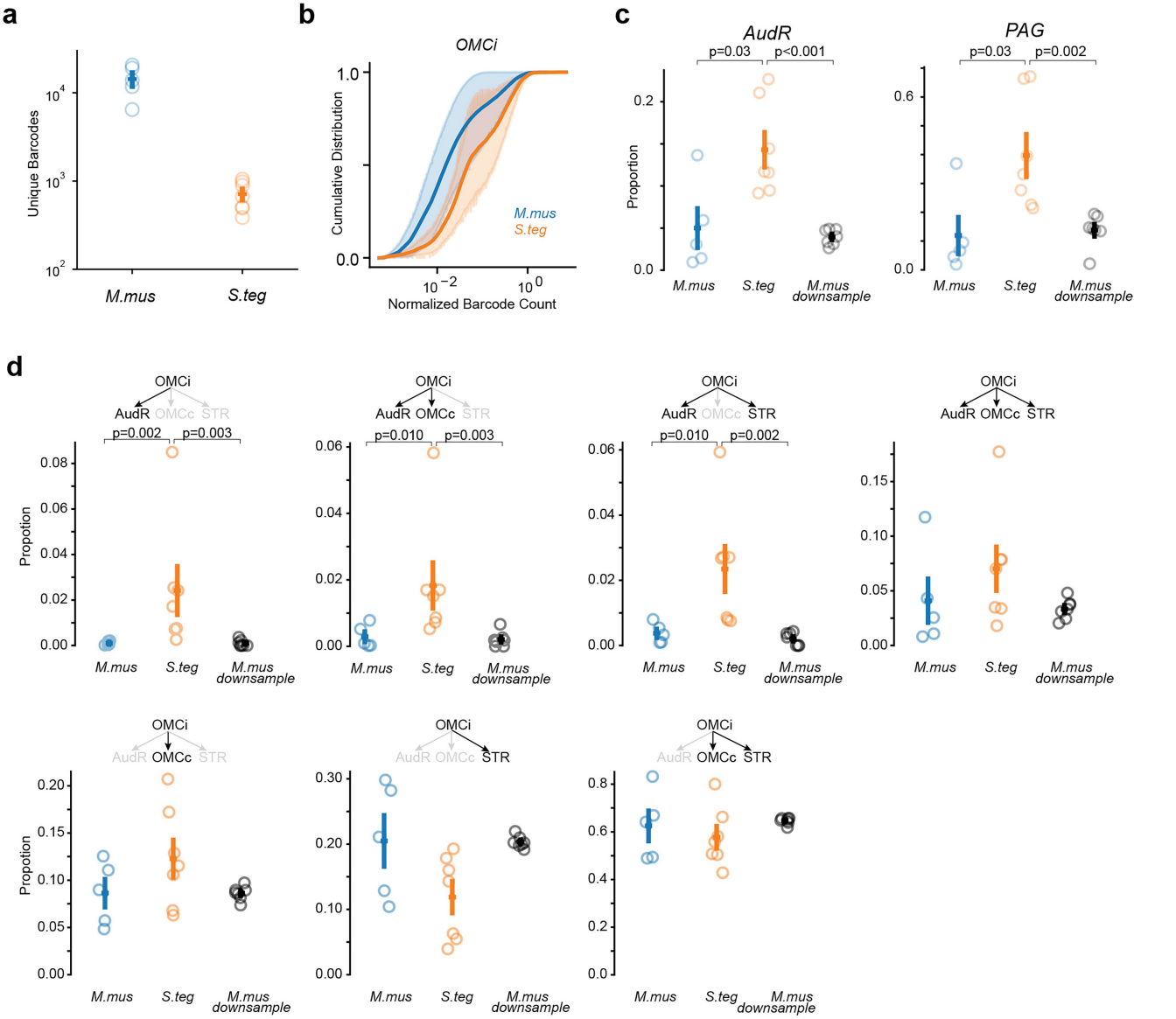

Extended Data Fig. 4 | Sindbis infectivity and downsampling of MAPseq data. (**a**) Number of unique barcodes recovered in the lab and singing mouse (*M.mus* = 14,000 ± 2500 barcodes per animal, 5 animals; *S.teg* = 700 ± 100 barcodes per animal, 7 animals). (**b**) Distributions of normalized barcode count in the injection site (OMCi) of lab (*blue*) and singing mice (*orange*) (*M.mus* = 0.04 ± 0.02 vs *S.teg* = 0.13 ± 0.04). Opaque lines and transparent margins represent the mean and s.e.m. of each species respectively. (**c**) Proportion of IT neurons that project to AudR (*left*) and proportion of PT neurons that project to PAG (*right*) (see Fig. 3f–h). Comparison is between lab mice, singing mice, and a downsampled population of lab mice IT or PT neurons (two-sided Mann-Whitney U test) (**d**) Proportion of IT motifs in lab mice, singing mice, and a downsampled population of lab mice IT neurons (two-sided Mann-Whitney U test). Box and vertical bars represent mean and s.e.m. respectively.

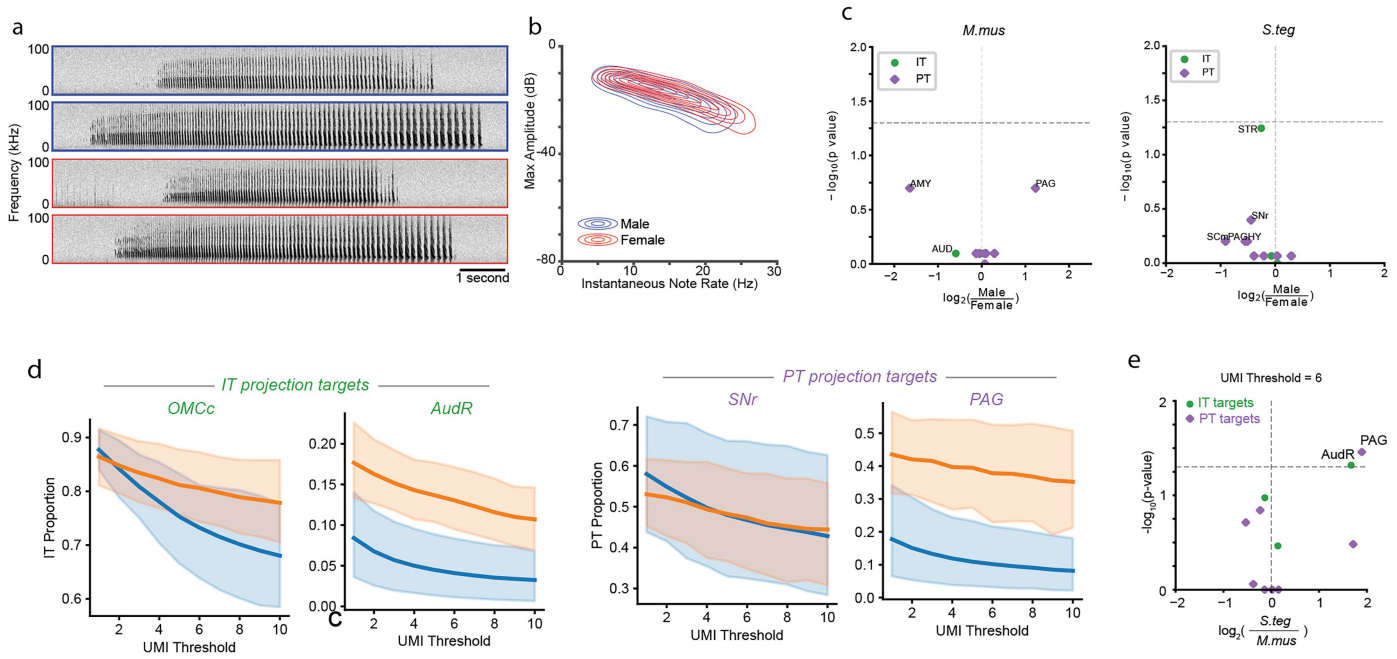

Extended Data Fig. 5 | Testing the effect of sex and varying UMI thresholds on projection proportions between species. (**a**) Example spectrograms of songs from male (*blue*) and female (*red*) singing mice. Time is plotted on the x-axis and pitch frequency is plotted on the y-axis. (**b**) The instantaneous note rate and max amplitude of every note from several songs are plotted with equidensity contours for notes made by male (*blue*) and female (*red*) singing mice (female n = 18091 notes, 181 songs; male n = 12154 notes, 102 songs). (**c**) Volcano plots showing the fold change of OMC projection probability means for different target regions between sexes in the lab mice (*left*) and singing mice (*right*). The y-axis shows the p-value as calculated by a two-sided Mann-Whitney U test. (**d**) Proportion of IT (*left*) or PT (*right*) neurons that project to select target regions given various UMI thresholds. A UMI threshold refers to the UMI count needed to determine the presence of a projection to a target region. Solid line is the mean and transparent fill is the s.e.m. across individuals within singing mice (*orange*) or lab mice (*blue*). (**e**) Volcano plots of fold change and p-value (two-sided Mann-Whitney U test) between species for all target regions given a UMI threshold of 6.

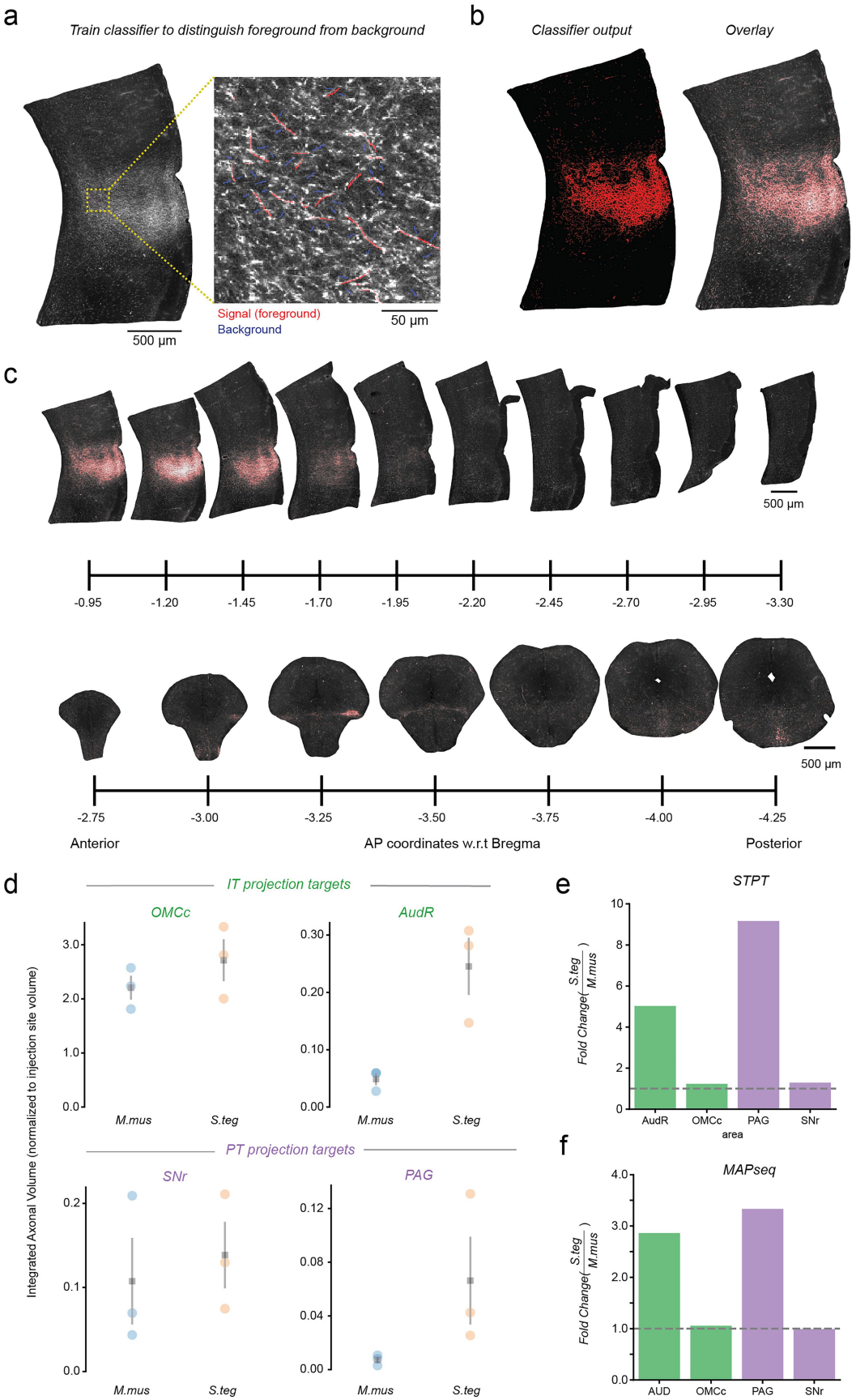

Extended Data Fig. 6 | See next page for caption.

Extended Data Fig. 6 | Quantification of STPT fluorescent data. (**a**) Example image of labelled data used for training of Labkit classifier. Red lines mark axonal fluorescent signal and blue lines mark background. The classifier was trained on select images from all individual mice to achieve comprable performance among all individuals. (**b**) The classifier is trained and applied across all images and outputs a segmented image (*left*, signal in red), which can be used to mask fluorescent signal (*right*). (**c**) Example images throughout the anterior-posterior axis of the AudR (*top*) and PAG (*bottom*) in a singing mouse. The segmented signal in red and overlayed with the raw image. (**d**) A volume of the segmented fluorescent signal within a target region was calculated and normalized to the injection site (OMCi) volume. Each dot refers to an individual mouse (3 lab mice, 3 singing mice). Mean and s.e.m. for each species is plotted in gray. (**e**) Fold change of normalized volume of fluorescent signal between singing and lab mice. (**f**) Fold change of OMC projection probability from MAPseq data. Same data as shown in Fig. 3g.

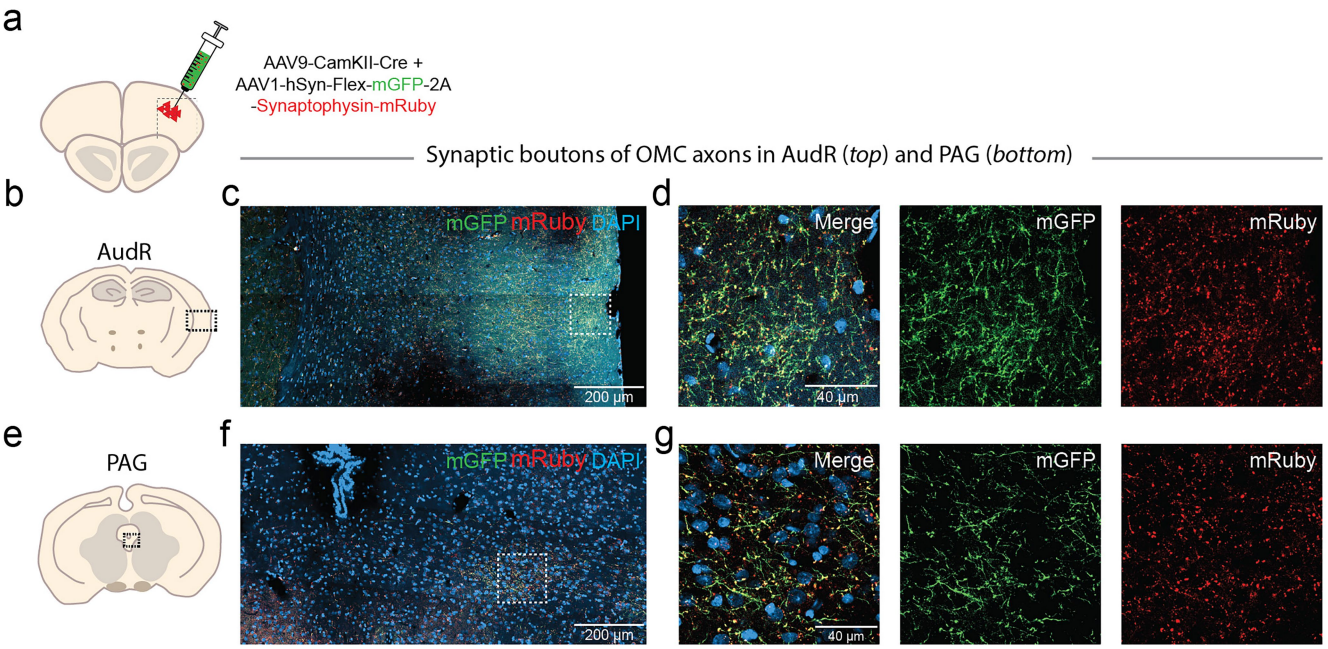

Extended Data Fig. 7 | Viral tracing of OMC synaptic boutons in target regions. (**a**) Virus expressing GFP, to visualize neuron processes, and synaptophysin tagged with mRuby, to visualize synaptic boutons, was injected into the OMC of a singing mouse. (**b**) Schematic of coronal slice imaged in c-d. (**c**) Confocal image of the injected singing mouse AudR showing OMC axons (*green*), OMC synaptic boutons (*red*), and nuclei (*blue*). (**d**) Zoom of dashed square region highlighted in c. (**e**) Schematic of coronal slice imaged in f-g. (**f**) Confocal image of the injected singing mouse PAG showing OMC axons (*green*), OMC synaptic boutons (*red*), and nuclei (*blue*). (**g**) Zoom of dashed square region highlighted in f. Experiments were performed on 2 singing mice with detected synaptophysin-mRuby in AudR and PAG of both animals.

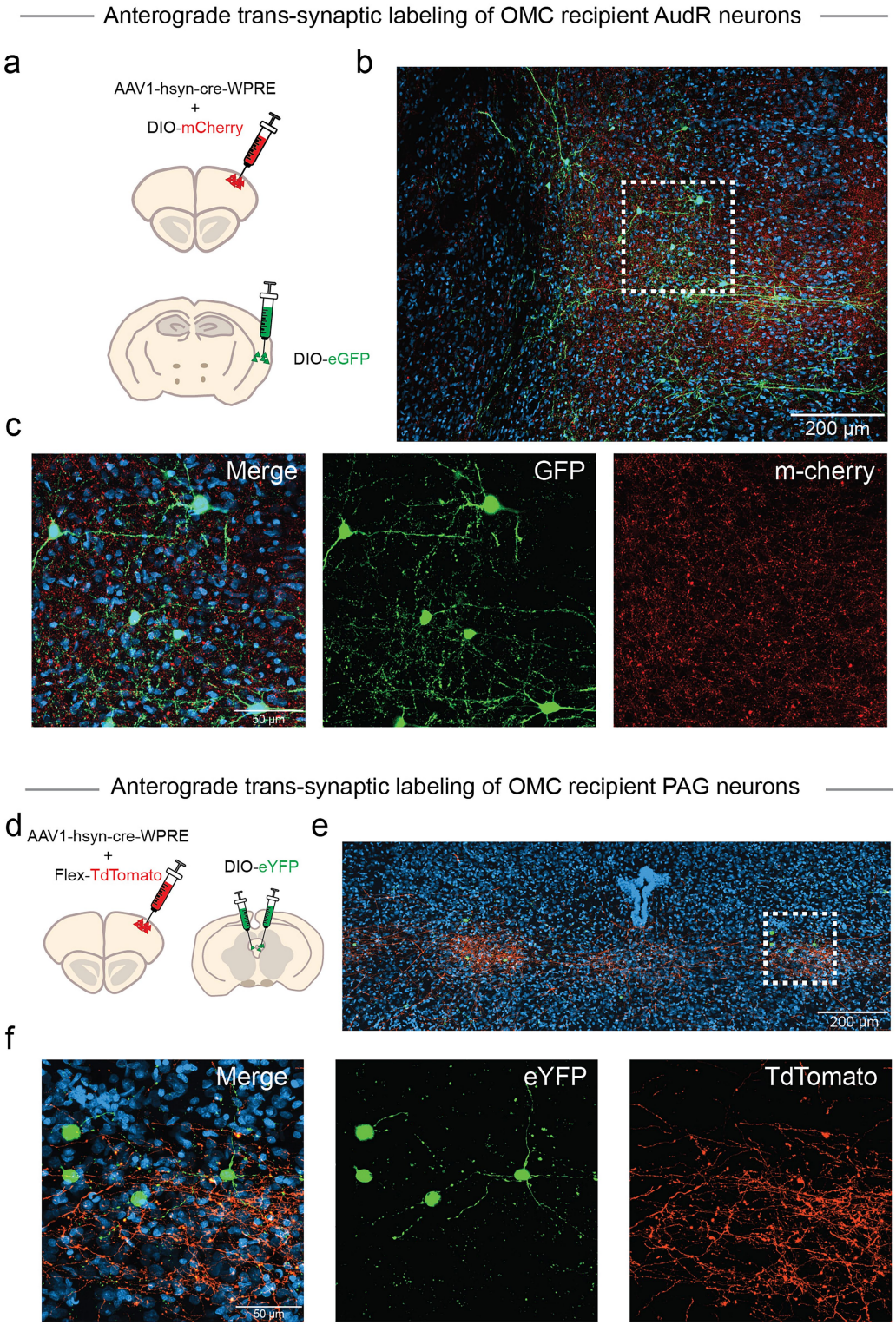

Extended Data Fig. 8 | Anterograde trans-synaptic tracing of OMC neurons. (**a**) An anterograde trans-synaptic AAV1 carrying cre was injected into the OMC in combination with a cre-dependent mCherry to visualize OMC axons. A cre-dependent eGFP was injected into the AudR in the same mouse. (**b**) Confocal imaging of the AudR region showing OMC axons (*red*), AudR neurons receiving OMC input (*green*), and nuclei (*blue*). (**c**) Zoom of dashed square region highlighted in b. (**d**) AAV1-cre was injected with cre-dependent TdTomato in the singing mouse OMC for anterograde trans-synaptic tracing of OMC output and to visualize OMC axons. A cre-dependent eYFP was injected bilaterally in the target region of PAG to visualize PAG neurons with OMC input. (**e**) Confocal imaging of the injected singing mouse PAG showing OMC axons (*red*), PAG neurons with OMC input (*green*), and nuclei (*blue*). (**f**) Zoom of dashed square region highlighted in e. Results shown here were replicated across 2 singing mice for each tracing experiment.

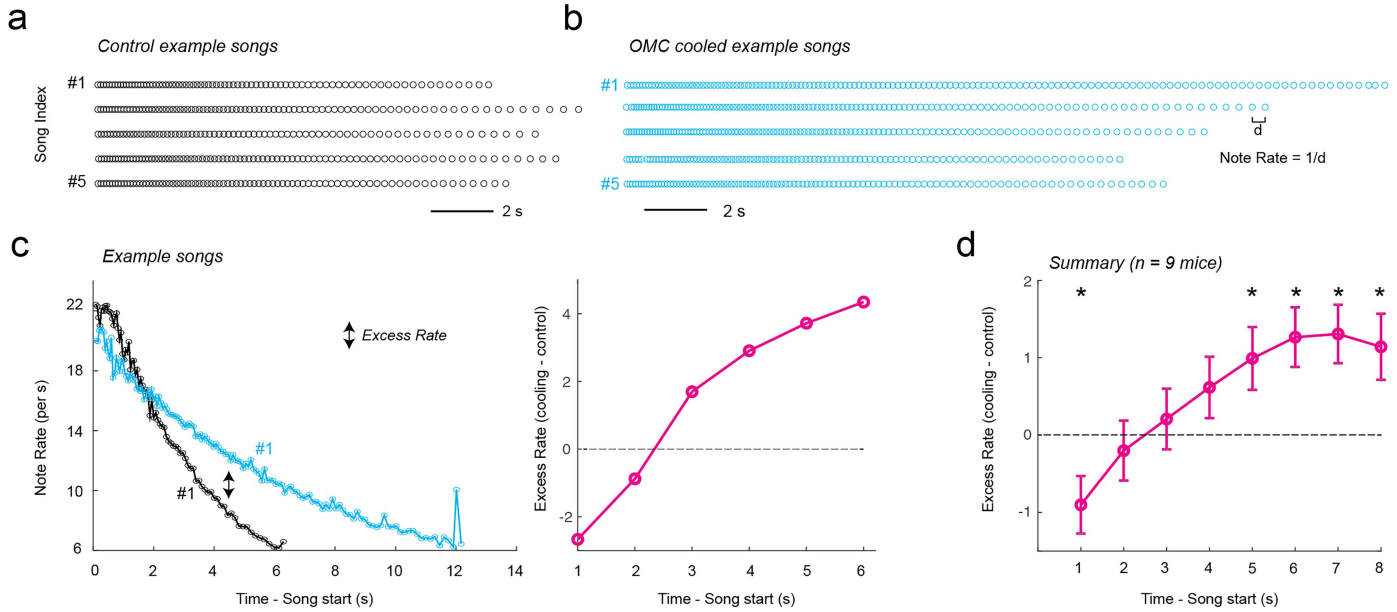

Extended Data Fig. 9 | Cooled OMC activity affects instantaneous note rate in singing mouse song. (a) Example singing mouse songs without temperature manipulation. Each row is an individual song and each open circle is a note within that song. **(b)** Example singing mouse songs when the OMC is cooled. Instantaneous note rate is defined as the reciprocal of the time between successive note onsets (*d*). **(c)** *Left*: Example song trajectories for 2 songs from one singing mouse are plotted by the instantaneous note rate on the y-axis and the time from the first note on the x-axis. Each dot corresponds to a note within the song. The first example songs from panels a and b are plotted. *Right*: The difference between the instantaneous note rates for a cooled (*left plot, blue*) and uncooled (*left plot, black*) song are plotted (*pink*). Bin size: 1 s **(d)** Differences in instantaneous note rates from cooled (n = 135 songs) and uncooled songs (n = 782 songs) from a total of 9 singing mice. Bin size: 1 s. Dots plotted correspond to the mean and error bars correspond to s.e.m. Asterisks indicate $P < 0.05$, under a two sample t-test.

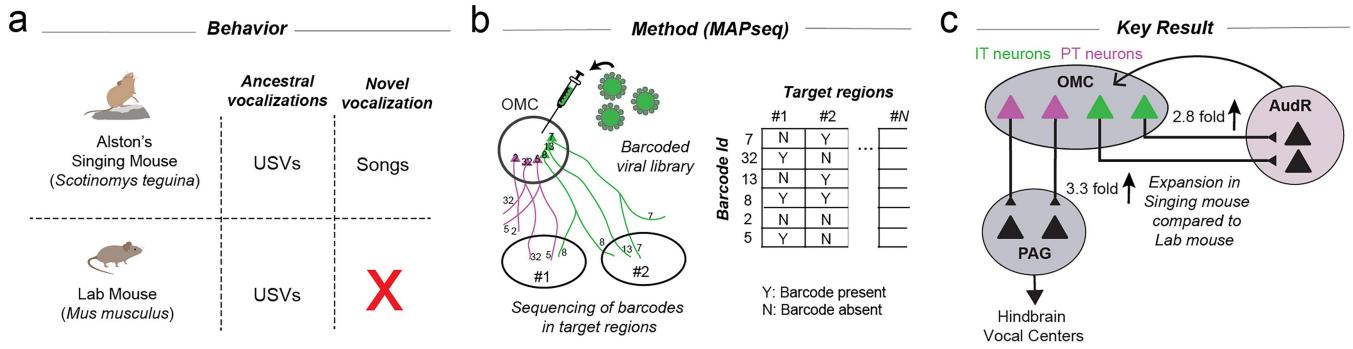

Extended Data Fig. 10 | Summary of findings. (**a**) Comparison of vocal behavior between singing mice and lab mice. (**b**) Schematic of MAPseq, where virus carrying unique RNA barcodes (represented by numbers) are injected into a region of interest (*left*). Downstream target regions are dissected and sequenced to identify the targets of each individual neuron (*right*). (**c**) Schematic showing the selective expansion of OMC IT neurons projecting to AudR and OMC PT neurons projecting to PAG in the singing mice compared to the lab mice.

nature portfolio

Corresponding author(s): Arkarup Banerjee

Last updated by author(s): Feb 9, 2026

Reporting Summary

Nature Portfolio wishes to improve the reproducibility of the work that we publish. This form provides structure for consistency and transparency in reporting. For further information on Nature Portfolio policies, see our Editorial Policies and the Editorial Policy Checklist.

Statistics

For all statistical analyses, confirm that the following items are present in the figure legend, table legend, main text, or Methods section.

n/a	Confirmed	
☐	☒	The exact sample size (*n*) for each experimental group/condition, given as a discrete number and unit of measurement
☐	☒	A statement on whether measurements were taken from distinct samples or whether the same sample was measured repeatedly
☐	☒	The statistical test(s) used AND whether they are one- or two-sided *Only common tests should be described solely by name; describe more complex techniques in the Methods section.*
☒	☐	A description of all covariates tested
☐	☒	A description of any assumptions or corrections, such as tests of normality and adjustment for multiple comparisons
☐	☒	A full description of the statistical parameters including central tendency (e.g. means) or other basic estimates (e.g. regression coefficient) AND variation (e.g. standard deviation) or associated estimates of uncertainty (e.g. confidence intervals)
☐	☒	For null hypothesis testing, the test statistic (e.g. *F*, *t*, *r*) with confidence intervals, effect sizes, degrees of freedom and *P* value noted *Give P values as exact values whenever suitable.*
☒	☐	For Bayesian analysis, information on the choice of priors and Markov chain Monte Carlo settings
☒	☐	For hierarchical and complex designs, identification of the appropriate level for tests and full reporting of outcomes
☐	☒	Estimates of effect sizes (e.g. Cohen's *d*, Pearson's *r*), indicating how they were calculated

Our web collection on statistics for biologists contains articles on many of the points above.

Software and code

Policy information about availability of computer code

Data collection	For confocal microscopy, Zeiss ZEN Blue 3.8.2 was used. For STPT, Tissuevision XXX was used. For behavioral data, Avisoft RECORDER 4.4.1 was used.
Data analysis	Behavior: MATLAB (ver. 09r2), USVSEG, DEEPSqueak. Images: QuPath (0.6.0), FIJI (2.16.0). STPT: Python (3.11.14), brainreg (1.0.14), napari (0.6.6). MAPseq: python (3.14.0), pandas (2.3.3), numpy (2.3.3), seaborn (0.13.2), upsetplot (0.9.0)

For manuscripts utilizing custom algorithms or software that are central to the research but not yet described in published literature, software must be made available to editors and reviewers. We strongly encourage code deposition in a community repository (e.g. GitHub). See the Nature Portfolio guidelines for submitting code & software for further information.

Data

Policy information about availability of data

All manuscripts must include a data availability statement. This statement should provide the following information, where applicable:

- Accession codes, unique identifiers, or web links for publicly available datasets
- A description of any restrictions on data availability
- For clinical datasets or third party data, please ensure that the statement adheres to our policy

All relevant data have been uploaded to Dryad (DOI: 10.5061/dryad.8kprr4z2p) and are freely available to download. These include barcode x target region matrices used to generate MAPseq results.

Research involving human participants, their data, or biological material

Policy information about studies with human participants or human data. See also policy information about sex, gender (identity/presentation), and sexual orientation and race, ethnicity and racism.

Reporting on sex and gender	*Use the terms sex (biological attribute) and gender (shaped by social and cultural circumstances) carefully in order to avoid confusing both terms. Indicate if findings apply to only one sex or gender; describe whether sex and gender were considered in study design; whether sex and/or gender was determined based on self-reporting or assigned and methods used.* *Provide in the source data disaggregated sex and gender data, where this information has been collected, and if consent has been obtained for sharing of individual-level data; provide overall numbers in this Reporting Summary. Please state if this information has not been collected.* *Report sex- and gender-based analyses where performed, justify reasons for lack of sex- and gender-based analysis.*
Reporting on race, ethnicity, or other socially relevant groupings	*Please specify the socially constructed or socially relevant categorization variable(s) used in your manuscript and explain why they were used. Please note that such variables should not be used as proxies for other socially constructed/relevant variables (for example, race or ethnicity should not be used as a proxy for socioeconomic status).* *Provide clear definitions of the relevant terms used, how they were provided (by the participants/respondents, the researchers, or third parties), and the method(s) used to classify people into the different categories (e.g. self-report, census or administrative data, social media data, etc.)* *Please provide details about how you controlled for confounding variables in your analyses.*
Population characteristics	*Describe the covariate-relevant population characteristics of the human research participants (e.g. age, genotypic information, past and current diagnosis and treatment categories). If you filled out the behavioural & social sciences study design questions and have nothing to add here, write "See above."*
Recruitment	*Describe how participants were recruited. Outline any potential self-selection bias or other biases that may be present and how these are likely to impact results.*
Ethics oversight	*Identify the organization(s) that approved the study protocol.*

Note that full information on the approval of the study protocol must also be provided in the manuscript.

Field-specific reporting

Please select the one below that is the best fit for your research. If you are not sure, read the appropriate sections before making your selection.

☒ Life sciences ☐ Behavioural & social sciences ☐ Ecological, evolutionary & environmental sciences

For a reference copy of the document with all sections, see nature.com/documents/nr-reporting-summary-flat.pdf

Life sciences study design

All studies must disclose on these points even when the disclosure is negative.

Sample size	For behavioral studies, each animal produces hundreds of USVs and tens of songs in a single hour. Therefore, we decided that 3-5 recording sessions of independent animals per species would be more than sufficient to detect differences in vocalizations. For whole brain imaging studies, we used 3 animals per species to average out individual differences. For MAPseq studies, our first round included 3 lab and 3 singing mice. Based on the number of recovered barcodes and infectivity differences across species, we subsequently added 2 lab mice and 4 singing mice to our dataset. This combined dataset was sufficiently powered for our analyses.
Data exclusions	Barcodes were excluded from MAPseq analysis if either 1) less than 30 barcode molecules were recovered at the injection site or 2) no target region had more than 5 barcode molecules. This threshold was determined to minimize false positives in the negative control region collected (olfactory bulb and hippocampus).
Replication	All behavioral, bulk viral tracing and MAPSeq data were independently replicated. Behavioral experiments were replicated across 5 singing mice and 5 lab mice. For whole-brain two-photon imaging, 3 animals were imaged for each species. Two rounds of MAPseq were completed using two different batches of animals with a total of 7 singing mice and 5 lab mice.
Randomization	Group allocation is not applicable in this study, as we did not compare across treatment conditions but static species characteristics.
Blinding	No blinding was done as there was no group allocation of treatment conditions.

Reporting for specific materials, systems and methods

We require information from authors about some types of materials, experimental systems and methods used in many studies. Here, indicate whether each material, system or method listed is relevant to your study. If you are not sure if a list item applies to your research, read the appropriate section before selecting a response.

Materials & experimental systems

n/a	Involved in the study
☒	☐ Antibodies
☒	☐ Eukaryotic cell lines
☒	☐ Palaeontology and archaeology
☐	☒ Animals and other organisms
☒	☐ Clinical data
☒	☐ Dual use research of concern
☒	☐ Plants

Methods

n/a	Involved in the study
☒	☐ ChIP-seq
☒	☐ Flow cytometry
☒	☐ MRI-based neuroimaging

Animals and other research organisms

Policy information about studies involving animals; ARRIVE guidelines recommended for reporting animal research, and Sex and Gender in Research

Laboratory animals	All animals used in this study were lab bred. Mus musculus animals of the strain C57BL/6J at 3-6 months of age were used. Lab bred animals of Scotinomys teguina at 3-6 months of age were used. Mice were housed on a 12:12 light:dark cycle, 20-22 degrees Celsius, and 30-70% humidity.
Wild animals	This study did not involve the use of any wild animals.
Reporting on sex	For experiments designed to determine sex differences (MAPseq), 2-4 animals of each sex were used. We did not find any significant differences between the sexes, so our findings report on the species, not sex, differences.
Field-collected samples	This study did not involve any field-collected samples.
Ethics oversight	All experiments were approved and conducted in accordance with the Cold Spring Harbor Laboratory Institutional Animal Care and Use Committee.

Note that full information on the approval of the study protocol must also be provided in the manuscript.

Plants

Seed stocks	*Report on the source of all seed stocks or other plant material used. If applicable, state the seed stock centre and catalogue number. If plant specimens were collected from the field, describe the collection location, date and sampling procedures.*
Novel plant genotypes	*Describe the methods by which all novel plant genotypes were produced. This includes those generated by transgenic approaches, gene editing, chemical/radiation-based mutagenesis and hybridization. For transgenic lines, describe the transformation method, the number of independent lines analyzed and the generation upon which experiments were performed. For gene-edited lines, describe the editor used, the endogenous sequence targeted for editing, the targeting guide RNA sequence (if applicable) and how the editor was applied.*
Authentication	*Describe any authentication procedures for each seed stock used or novel genotype generated. Describe any experiments used to assess the effect of a mutation and, where applicable, how potential secondary effects (e.g. second site T-DNA insertions, mosiacism, off-target gene editing) were examined.*